Assessing Locations Susceptible to Shallow Landslide Initiation During Prolonged Intense Rainfall in the Lares, Utuado, and Naranjito Municipios of Puerto Rico

Rex L. Baum[1], Dianne L. Brien[2], Mark E. Reid[2], William H. Schulz[1], and Matthew J. Tello[1,3]

[1]U.S. Geological Survey, Golden, Colorado 80401, USA [2]U.S. Geological Survey, Moffett Field, California 94035, USA

[3]Present Address, Colorado Department of Transportation, Denver, Colorado 80204, USA

Correspondence to: Rex L. Baum (baum@usgs.gov)

Abstract. Hurricane María induced about 70,000 landslides throughout Puerto Rico, USA, including thousands each in three municipalities situated in Puerto Rico's rugged Cordillera Central range. By combining a nonlinear soil-depth model, presumed wettest-case pore pressures, and quasi-three-dimensional (3D) slope-stability analysis we developed a landslide susceptibility map that has very good performance and continuous susceptibility zones having smooth, buffered boundaries. Our landslide susceptibility map enables assessment of potential ground-failure locations and their use as landslide sources in a companion assessment of inundation and debris-flow runout. The quasi-3D factor of safety, F_3, showed strong inverse correlation to landslide density (high density at low F_3). Area under the curve (AUC) of True Positive Rate (TPR) versus False Positive Rate (FPR) indicated success of F_3 in identifying head-scarp points (AUC=0.84) and source-area polygons ($0.85 \leq$ AUC ≤ 0.88). The susceptibility zones enclose specific percentages of observed landslides. Thus, zone boundaries use successive F_3 levels for increasing TPR of landslide head-scarp points, with zones bounded by F_3 at TPR=0.75, very high; F_3 at TPR=0.90, high; and the remainder moderate to low. The very high susceptibility zone, with 118 landslides/km^2, covered 23% of the three municipalities. The high zone (51 landslides/km^2) covered another 10%.

1 Introduction

Landslide susceptibility maps are widely used to mitigate the major hazards landslides pose to people, public and private property, lifelines, utilities, and businesses. Reliable application of physically based models to landslide susceptibility assessment has been intensively researched since the 1990s. Many models and computer codes for such assessments exist (Montgomery and Dietrich, 1994; Wu and Sidle, 1995; Pack et al. 1998; Simoni et al. 2008; Baum et al. 2010; Arnone et al. 2011; Rossi et al. 2013). Nevertheless, several scientific and technical challenges complicate the application of these models over large areas. These challenges exist, in part, because many geological, hydrological, and geotechnical details of the subsurface remain unknowable except at points of direct observation. Among others, the subsurface knowledge gaps include (1) relationships between soil thickness and shallow landslide depth, (2) model parameter spatial distribution and variability, (3) pore pressure and effective stress distributions, and (4) landslide failure modes. Research has made much progress in addressing these knowledge gaps. For example, many physically based and empirical soil-depth models are available (Roering, 2008; Pelletier and Rasmussen 2009; Ho et al. 2012; Catani et al. 2010; Nicótina et al. 2011; Gomes et al. 2016; Patton et al. 2018, Yan et al. 2021; Xiao et al., 2023), making it possible to estimate the field-distribution of soil depth in landslide prone areas (Godt et al. 2008a; Segoni et al. 2009; Ho et al. 2012). Some studies have combined field or laboratory measured properties with mapped lithologic characteristics and statistical analysis to describe the spatial distribution of soil properties (Godt et al. 2008b; Tofani et al. 2017). Many other studies have applied probabilistic approaches successfully to address parameter uncertainty and improve accuracy of physically based modelling of landslide susceptibility (Raia et al. 2014; Zieher et al. 2017; Canli et al. 2018; Palacio Cordoba et al. 2020; Medina, et al. 2021). Despite these advances, accurate assessment of landslide susceptibility using physically based methods remains difficult.

Most physically based landslide susceptibility models have relied on the one-dimensional (1D) infinite-slope analysis to model slope-stability. This approximation is suitable for representing shallow landslides in raster-based topography where the resolution (grid-cell spacing) is tens of meters. However, applying the 1D analysis to high-resolution (a few

meters or less) topography violates the 1D assumptions of laterally uniform stress and a planar failure surface. A few spatially distributed three-dimensional (3D) (Mergilli et al. 2014a, 2014b; Reid et al. 2015) and quasi-3D (von Reutte et al. 2013; Milledge et al. 2015) methods have become available to overcome limitations of the 1D analysis. In the quasi-3D method of von Reutte et al. (2013) soil columns interact with their neighbors and load is redistributed when driving forces at the base of a column exceed basal strength. Milledge et al. (2015) used a search algorithm to identify patches of potentially unstable grid cells by assuming driving forces acting on a group of cells exceed the resisting forces at the group's margins and that cell groups act as rigid blocks with a failure surface at the soil-bedrock interface. Mergilli et al. (2014a, 2014b) assumed 3D landslide geometry based on ellipsoidal failure surfaces and used Hovland's (1977) force-equilibrium method to analyze stability across a digital landscape. Reid et al (2015) used spherical trial surfaces with moment-equilibrium analysis methods, which tend to be more accurate than methods based on force equilibrium alone.

The main objective of this work is to produce integrated maps of potential landslide initiation and inundation areas. Secondary objectives are to integrate soil-depth modeling, consideration of parameter variability, and quasi-3D slope stability analysis into our assessments. Our approach to soil-depth modeling achieves a good compromise between swift, simple methods (constant depth or simple empirical methods, such as DeRose et al. 1991) and the most complicated and computationally intensive (Xiao et al. 2023). Likewise for our quasi-3D slope stability analysis. Although much progress has been made in methods for assessing landslide susceptibility (e.g., Carrara et al. 1999; Chung and Fabri 2003; Lee et al. 2003; Godt et al. 2008; Baum et al. 2014; Canli et al. 2018) as well as debris-flow inundation (George and Iverson 2014; Reid et al. 2016; Aaron et al. 2017; Bessette-Kirton et al. 2019b), combining these two types of assessments into a single map for an area of hundreds of square kilometers remains challenging (Ellen et al. 1993; Benda et al. 2007; Fan et al. 2017; Hsu and Liu 2019; Mergili et al. 2019). As noted previously, one of the challenges is estimating potential source-area extent and depth. We addressed this challenge by modelling soil depth and using it to approximate potential source-area depth in 1D and quasi-3D slope stability models for use in assessing regional shallow landslide susceptibility. Such an approach helps ensure that the susceptibility model accounts for variable failure depth across the landscape and that predicted areas of potential landslide sources are acceptable for use in assessing debris-flow inundation. We compared results of several soil-depth models to find the one that performed the best in our study area. The quasi-3D model uses a simplified limit-equilibrium analysis to estimate the stability of a slab- or goldpan-shaped trial landslide. Another challenge is establishing meaningful susceptibility categories, which we addressed by delimiting the categories at quasi-3D factor of safety values, F_3, that enclose specific percentages of landslide sources, rather than relying on theoretical or arbitrary factor of safety values to delimit the categories. By showing like outcomes (areas that capture specific percentages of observed landslides), maps based on this approach are directly comparable to each other.

In the aftermath of Hurricane María, the U.S. Geological Survey (USGS) began working with local partners to conduct detailed assessments of landslide and debris-flow hazards, both island-wide (Bessette-Kirton et al. 2017; Hughes and Schulz 2020a, b) and more locally (this study) for three impacted municipalities (Lares Municipio, Utuado Municipio, and Naranjito Municipio) in the central mountains of Puerto Rico (Fig. 1). These municipalities were an ideal location for testing and developing methods for such assessments. Here we describe the landslide initiation (source area) part

of a landslide susceptibility assessment for these municipalities. Estimating landslide initiation potential is part of a larger effort (in progress, Brien et al. 2021) to estimate overall hazard from (1) landslide initiation (ground failure), (2) landslide runout, and (3) debris-flow inundation from future extreme rainfall, including tropical cyclones (hurricanes), as well as localized storms expected to impact these areas of Puerto Rico.

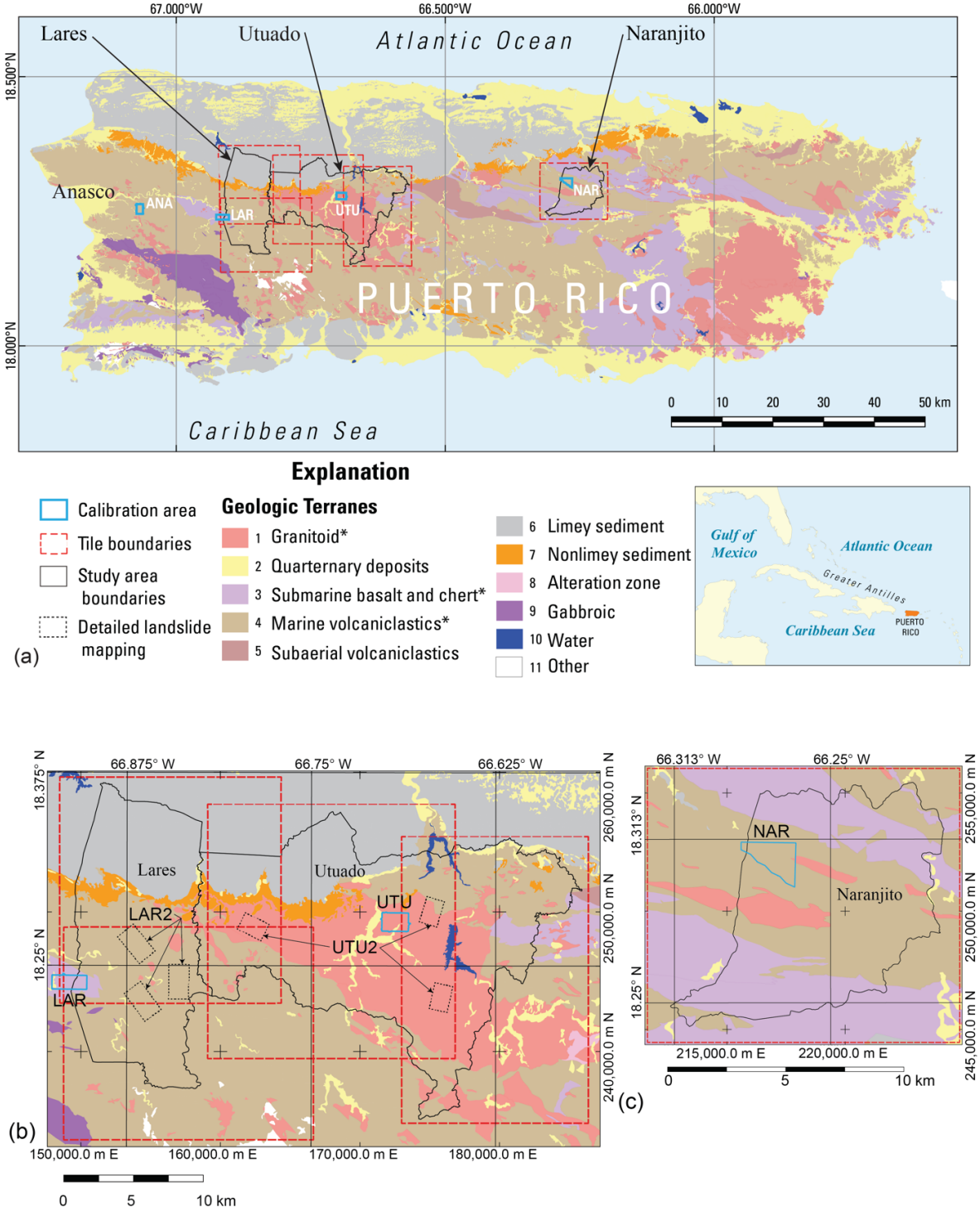

Figure 1. Geologic map showing municipality boundaries, study areas, calibration areas, and major lithologies (geologic terranes) for the main island of Puerto Rico. Simplified from Bawiec (1998) by combining submarine volcaniclastic rocks of various ages into a single map unit. Primary landslide-prone lithologies indicated by * in map explanation. Municipality boundaries of Lares, Utuado, and Naranjito define study areas. Digital elevation models covering the study areas were divided into five smaller tiles. Extent of Añasco (ANA), Lares (LAR), Utuado (UTU), and Naranjito (NAR) calibration areas from landslide inventories by Bessette-Kirton et al. (2019c, 2020). (a) overview of entire island, (b) details of Lares and Utuado study areas including outlines of areas of detailed landslide mapping in Utuado, (UTU2, Einbund et al. 2021a) and Lares (LAR2, Einbund et al. 2021b), (c) details of Naranjito study area.

In the following sections, we describe characteristics of the study areas, summarize our methods and results, and discuss advantages, limitations, and implications of our approach. First, we describe the setting, geology, and landslides of Puerto Rico including details specific to the study areas. Then we describe the available topographic and geotechnical data followed by a description of the workflow for assessing landslide susceptibility. Next, we describe our methods for modelling soil depth, pressure head, and slope stability along with procedures for model calibration and details of how the calibrated models were applied to and evaluated for our study areas. Then we present results of the calibration, soil-depth modelling, 1D and quasi-3D stability analyses, and the evaluation and validation of the susceptibility analysis. These results were obtained using pre-event light detection and ranging (lidar) bare-earth digital elevation models (DEM) (U.S. Geological Survey, 2018). The DEMs, with uniformly spaced elevation values, were created from ground returns of lidar point clouds. DEMs are known in some countries as digital terrain models, a term with two definitions; throughout this paper we use DEM to avoid ambiguity (Heidemann, 2018). We reran our models using calibrated input parameters and post-event lidar (U.S. Geological Survey 2020a, b, c) to estimate susceptibility to future landslides. We finish by discussing strengths and limitations of our approach as well as some unexpected findings and ways to simplify the workflow for application to areas where limited data are available.

2 Study area

Puerto Rico is a U.S. territory and lies at the east end of the Greater Antilles island chain in the Caribbean Sea (Fig. 1). The main island is characterized by rugged topography and covers an area of 8750 km^2. The study areas and calibration areas lie in the east–west-trending Cordillera Central range, which spans most of the island. The range exceeds elevations of 900 m at many places, and its highest peak reaches an elevation of 1340 m. Coastal plains and broad lowlands ring most of the island. Ongoing tectonic uplift is one of the main factors creating the rugged topography across the island (Taggart and Joyce 1991). Warm temperatures, high rainfall, and humidity contribute to deep weathering and widespread saprolite formation (Murphy et al. 2012).

This study was conducted in stages between 2018 and 2022 and involved three study areas as well as calibration areas, study-area tiles, and validation areas. We define these here to help the reader comprehend how our presentation of the study is organized. The study areas comprise three municipalities, Lares Municipio, Utuado Municipio, and Naranjito Municipio, and are the focus of our landslide initiation susceptibility maps (Supplemental Figures S1 and S2; Baum et al. 2023). These municipalities were chosen because they were severely impacted by Hurricane María landslides and to help manage their future growth and development. We enclosed the Lares and Utuado study areas in four overlapping rectangles and enclosed Naranjito Municipio in a fifth, separate rectangle (Fig. 1a, 1b, and 1c). The rectangles extend beyond the drainage divides of basins that straddle municipality boundaries. The rectangles delimit

overlapping tiles of the DEM used in the susceptibility analysis. These DEM tiles helped keep file sizes (6 gigabytes or less for ASCII input and output grids) manageable and overlap ensured that edge effects would not degrade soil-depth or slope-stability computations. The extended boundaries ensured that landslide runout and debris-flow inundation models (Brien et al. 2021) would not be impeded by municipality boundaries or other artificial barriers. The calibration areas (Fig. 1) were placed in distinct geologic terranes where high concentrations of landslides had occurred. Previous detailed mapping and characterization (Bessette-Kirton et al. 2019c, 2020) and field studies (Baum et al. 2018) in these areas provided data for testing and calibrating soil-depth and slope-stability models (Tello 2020). From east to west, each 2-km^2 calibration area was named for a nearby city: Añasco (ANA), Lares (LAR), Utuado (UTU), and Naranjito (NAR). Although ANA is about 15 km west of the study areas, it was included to provide additional calibration data in an area of high landslide density for submarine volcaniclastic lithologies because sufficient data were not available at NAR. Soils, land cover, and other characteristics (besides bedrock lithology) that influence landslide susceptibility vary between the four calibration areas (Bessette-Kirton et al. 2020; Hughes and Schulz 2020a, 2020b). We used six additional areas of detailed mapping (Einbund et al. 2021a, 2021b) to help evaluate the final maps. These validation areas are designated LAR2 and UTU2, and each includes three rectangular areas of detailed landslide mapping. (Fig. 1b). We combined detailed source area mapping of NAR (Baxstrom et al. 2021a) and UTU (Einbund et al. 2021a) with that in LAR2 and UTU2 for the validation.

2.1 Geology and soils

Heavily faulted basement rocks, consisting mainly of oceanic crust, volcaniclastic, and intrusive rocks, underlie the Cordillera Central range (Jolly et al. 1998). A cover sequence of carbonates and associated clastic sediments unconformably overlies the basement complex. The carbonates have weathered to form tropical karst in the lowlands north of the range (Monroe 1976). Bawiec (1998) generalized the geology of Puerto Rico into twelve geologic terranes having related rock types. We have simplified the terranes slightly for purposes of this study (Fig. 1). Soil mapping and databases published by the U.S. Department of Agriculture's Natural Resources Conservation Service (NRCS) indicate a wide range in the textures (particle-size distributions) and hydraulic properties of soils in the study areas (Soil Survey Staff 2018). Most hillside soils have developed by in-place chemical weathering of underlying bedrock or saprolite and locally derived colluvium. Despite the steep slopes, in many places the upper few meters of bedrock have weathered to saprolite (e.g., Jibson 1989; Larsen and Torres-Sanchez 1992).

2.2 Landslides

Heavy rainfall from Hurricane María during September 2017 produced tens of thousands of landslides on the main island of Puerto Rico, USA (Bessette-Kirton et al. 2017, 2019a; Hughes et al. 2019). Shallow, translational failures in soil or saprolite, from decimeters to a few meters deep were the most common landslides. Deeper (up to 30 m) complex failures in soil, saprolite, and rock, as well as rock falls and rock slides also occurred (Bessette-Kirton et al. 2017). Many landslides transformed into debris flows that commonly coalesced and flowed down channels. Landslides caused fatalities as well as widespread damage to homes, roads, and other infrastructure.

Recent and historical studies described and characterized Puerto Rico's rainfall-induced landslides. Published studies of past landslides characterized rainfall-induced landslides in southern and eastern parts of Puerto Rico (Jibson 1989; Simon et al. 1990; Larsen and Torres-Sanchez 1992, 1998; Pando et al. 2005; Larsen 2012). Several post-Hurricane María studies documented dimensional, geologic, and topographic characteristics of landslide sources in ten representative areas of high landslide density within and near the municipality study areas (Fig. 1): Baum et al. (2018) conducted field studies and measurements (Fig. 2), and Bessette-Kirton et al. (2019c) later mapped landslides using post-event aerial photography in the four areas denoted as ANA, LAR, NAR, and UTU (Fig. 1a). U.S. Geological Survey staff later remapped NAR (Baxstrom et al. 2021a), remapped UTU (Einbund et al. 2021a), and mapped six additional areas (UTU2 and LAR2, Fig. 1b) near UTU and LAR (Einbund et al. 2021a, 2021b). Schulz et al. (2023) expanded on earlier field studies of Baum et al. (2018). Data from some of these studies supported recent analyses of landslide susceptibility (Bessette-Kirton et al. 2019a; Hughes and Schulz 2020a) and runout characteristics (Bessette-Kirton et al. 2020).

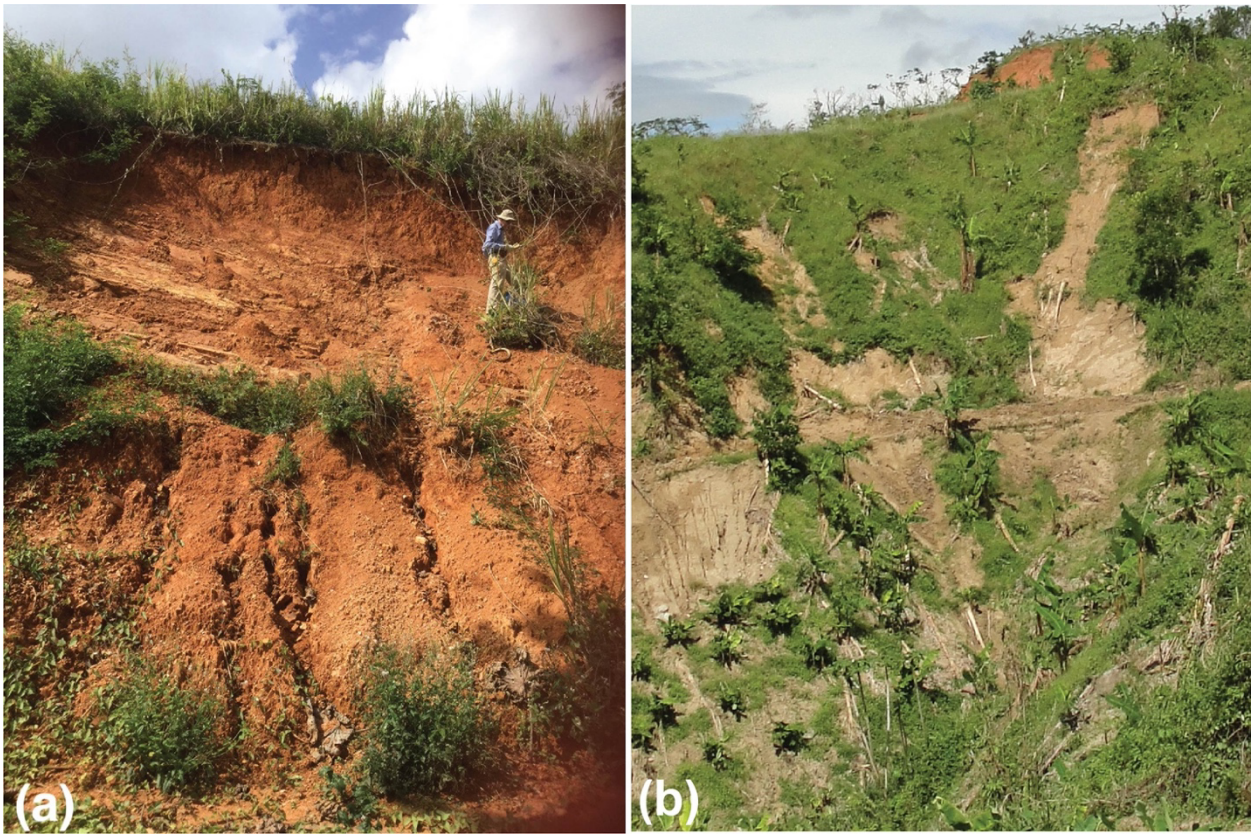

Figure 2. Photographs depicting source areas of shallow landslides in (a) volcaniclastic terrane (photograph by C. Cerovski-Darriau, U.S. Geological Survey, May 2018, public domain) and (b) granitoid terrane one month after Hurricane María (photograph by W. Schulz, U.S. Geological Survey, October 2017, public domain).

The post-Hurricane María studies cited above indicated that most source areas were fully evacuated, and shallow translational slides appear to be the most common type of movement prior to transforming to debris flows. Nevertheless, source area shapes were consistent with translational, rotational, or complex movement. Source areas exposed soil, saprolite, and bedrock (Fig. 2). Soil matrix textures ranged from sand to clay; clast content increased

with depth. Differences between the landslide source sizes and depths within the different terranes (Fig. 3) seem consistent with their different lithologies and depth of weathering (volcaniclastic rocks, weathered volcanic rocks, granitic pluton).

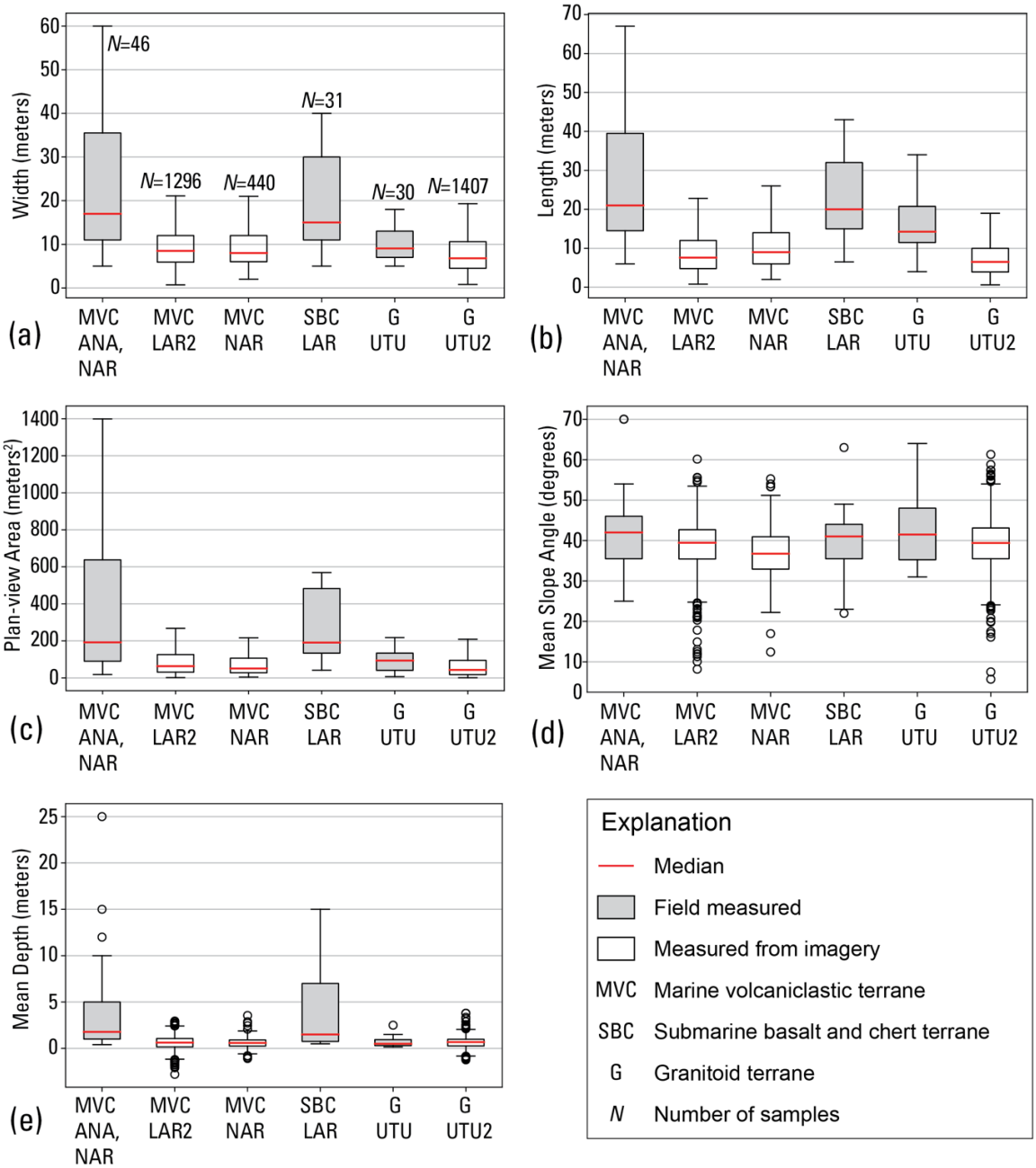

Figure 3. Box plots summarizing landslide source dimensions obtained for three geologic terranes by field studies of 107 landslides (gray, Baum et al. 2018) and by mapping 3440 landslides from aerial imagery and lidar-derived digital elevation models (white, Baxstrom 2021a; Einbund 2021a, 2021b). (a) width, (b) length, (c) plan-view area calculated directly by geographic information system for mapped polygons and estimated from field measurements as an ellipse and projected to the horizontal, π × (Length × Width × cos (Slope angle))/4, (d) mean slope angle, (e) mean landslide source depths. Outliers of width, length and area not shown to keep 25%, 50%, and 75% quartiles legible; box length = interquartile range (IQR),

whiskers = 1.5 x IQR. [Locations (as shown in Fig. 1): ANA, Añasco; LAR, Lares; LAR2, Lares (Einbund et al. 2021b); UTU, Utuado; UTU2, Utuado (Einbund et al. 2021b, includes UTU); NAR, Naranjito (remapped by Baxstrom et al. 2021a)].

Figure 3 summarizes landslide dimensions obtained from the post-Hurricane María studies for the three main geologic terranes in the study areas (Fig. 1). The field measurements (using laser range finder, tape, and clinometer; Baum et al. 2018), though biased by purposely including several large landslides (1500 m^2 – 6600 m^2), represent the range of sizes of Hurricane María landslide sources. Mapping from imagery (Baxstrom et al. 2021a; Einbund et al. 2021a, 2021b) included all landslides visible in the imagery of several 2.5-km^2 target areas and represent typical dimensions of landslides triggered by the hurricane on uplands and valley side slopes. Most landslide sources had lengths and widths less than 10-15 m, with median mapped length and width among the different samples in Figure 3a, 3b ranging from 6.5 m to 9 m. Many landslide sources have areas less than 100 m^2 (median mapped areas range from 42 m^2 to 64 m^2 for the different terranes), and very few have areas greater than 1000 m^2 (Fig. 3c). Although landslides occurred on a wide range of slope angles, most occurred on slopes between 30º and 50º (Fig. 3d). Median DEM-derived mean slope angles of mapped landslide sources were 37° - 39° (Fig. 3d). Depths computed by differencing pre-event and post-event lidar elevation data (Baxstrom et al. 2021a; Einbund et al. 2021a, 2021b) have significant uncertainty because 14 – 19% of the landslide sources had mean and median elevation differences indicating net gain of material (Fig. 3e). In addition, undisturbed areas outside the landslide polygons showed elevation differences that varied horizontally, consistent with inadequate swath adjustment in the pre- and post-event lidar point clouds. Data needed to correct the resulting mismatch between pre- and post-event lidar were unavailable. However, it seems unlikely that any of the mapped landslides had a mean depth much greater than 5.8 m (the span between the greatest elevation loss and gain, MVC/LAR2, Fig. 3e). Rare, large landslides had depths as great as 25 m according to field measurements (Fig. 3e).

Puerto Rico's complex geology (Fig. 1), tropical soils, rugged terrain, land use, and landcover exert strong influences on landslide susceptibility. Lepore et al. (2012) in an island-wide assessment using frequency ratio and logistic regression concluded that aspect, slope, elevation, geological discontinuities, and geology, were “highly significant landslide-inducing factors”; land cover and distance from roads were also significant. Bessette-Kirton et al. (2019a) showed that antecedent soil moisture was statistically correlated to densities of Hurricane-María-induced landslides and found that high landslide densities were “especially widespread across some geologic formations,” although the degree to which rainfall characteristics resulted in this correlation remained unclear. In a later post-Hurricane María, island-wide assessment using the frequency ratio method, Hughes and Schulz (2020a) found after accounting for the effects of soil moisture, there were strong correlations between landslides and slope, curvature, geologic terrane, mean annual precipitation, land cover, soil type, event soil moisture, proximity to roads, and proximity to fluvial channels for the Hurricane María event. Previous, more localized studies considered fewer geomorphic and geographic characteristics to classify landslide susceptibility using empirical and statistical methods (Larsen and Parks 1998; Larsen et al. 2004). For example, Larsen and Parks (1998) classified landslide susceptibility of Comerío Municipality based on elevation, slope, aspect, and land use. Our current study uses physics based geotechnical models of slope stability to directly assess topographic, geologic, and soil controls on landslide potential and to indirectly assess effects of roads and land use through their impacts on topography and surface drainage as expressed in the DEM as local changes in the slope characteristics.

3 Methods and materials

To represent the aerial extent and depths of potential landslide source areas, we undertook a multistage process to acquire data, characterize the landslides, calibrate parameters, and model potential landslide sources for both pre-Hurricane María and post-Hurricane María digital topography. In Figure 4, bold capital letters mark the four main stages of the study: (A) Data acquisition and reduction, (B) Calibration, (C) Susceptibility modeling on pre-storm topography, and (D) Susceptibility modeling on post-storm topography. Each stage comprises multiple steps; numbers in Fig. 4 identify the section describing each major step. Most results of Stage A were published previously, but are described briefly in sections 2.2, 3.1, and 3.2 to provide context for this study. Stages B, C, and D (Fig. 4) repeated four distinct modelling tasks: (1) soil depth, H, (2) pressure head, ψ, (3) 1D factor of safety, F_1, (4) quasi-3D factor of safety, F_3. The landscapes of the calibration and study areas were represented digitally in the models as raster grids based on 1-m-resolution pre-event lidar-derived DEMs. Each grid cell represented a column of potential landslide material of vertical depth, H, determined at soil-depth modelling steps of stages B, C, and D (Fig. 4). Computed soil depth from these steps became input for calculation of ψ, (Fig. 4); then H and ψ became inputs for computing F_1 (Fig. 4) and F_3. F_1 was used primarily in evaluating soil-depth models and shear-strength parameters for the calibration areas depicted in Fig. 1 using receiver operating characteristic (ROC, Metz, 1978) analysis (Fig. 4). During post-calibration slope-stability modelling of the study areas, F_1 served as a rough check on the computed value of F_3. The following sections outline the major steps depicted in Figure 4.

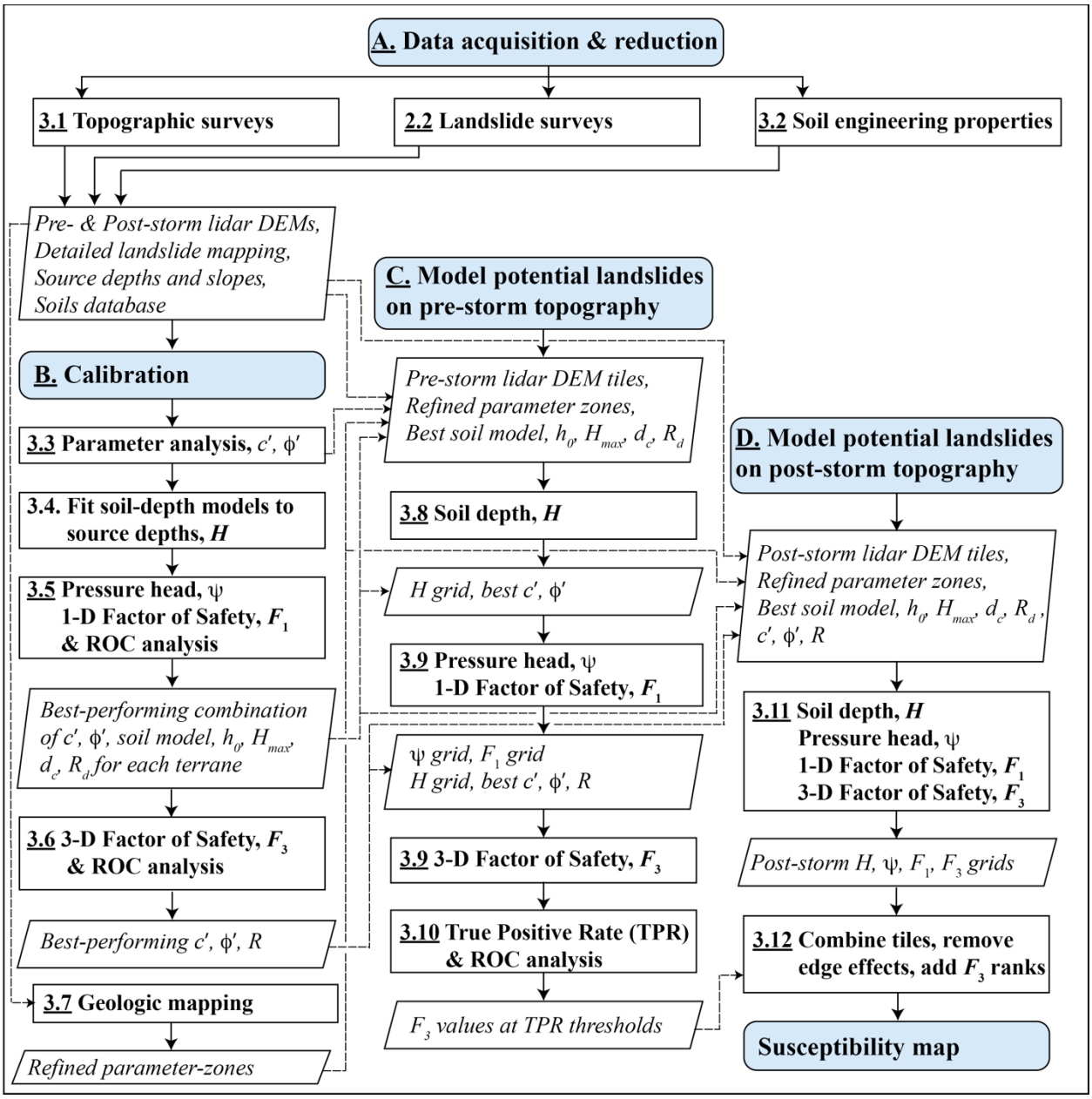

Figure 4. Flow chart showing four major stages (enumerated by capital letters A, B, C, D) and steps of data acquisition, calibration and modelling leading to the map of landslide initiation susceptibility (Susceptibility map, bottom of right column). Numbers (underlined, bold) identify the corresponding sections where the steps and their outputs are described. The data acquisition stage (A, top) was performed at scales ranging from island-wide to site specific. The calibration stage (B, left column) was performed using digital elevation models of roughly 2.5-km^2 areas where detailed mapping and fieldwork had been conducted (Fig. 1). Landslide source depths approximated soil depth for soil-depth model calibration. The pre-Hurricane María (pre-storm) modeling stage (C, center column) was conducted using overlapping DEM tiles (Fig. 1) derived from pre-Hurricane María lidar data (U.S. Geological Survey, 2018). The post-Hurricane María (post-storm) modeling stage (for generating map of future landslide susceptibility, D, right column) used overlapping DEM tiles (Fig. 1) derived from post-Hurricane María lidar data (U.S. Geological Survey, 2020a, b, c). Post-Hurricane María steps used identical input parameters to the corresponding pre-Hurricane María steps. [Chart symbols: Light-blue rounded rectangles, terminals of each major stage; rectangles with bold text, technical or computational processes; parallelograms with italic text, inputs or outputs; dashed lines, connections between outputs and model inputs. Model outputs: H, soil depth; ψ, pressure head; F_1, 1D factor of safety; F_3, quasi-3D factor of safety; TPR, true positive rate; ROC, Receiver Operating Characteristics. Model input parameters: h_0, characteristic soil depth, H_{max}, maximum soil depth; δ_c, critical

slope angle; R_d, diffusivity ratio; c', cohesion for effective stress; ϕ', angle of internal friction for effective stress; R, radius of quasi-3D trial surface.]

3.1 Topographic surveys and data

In 2015 and 2016, the U.S. Geological Survey (2018) acquired airborne lidar covering the entire main island of Puerto Rico. These data were processed to create a 1-m resolution bare-earth DEM. Referred to hereafter as pre-event lidar, these data were acquired roughly one to two years before Hurricane María and constitute the best available representation of topographic conditions before the landslides associated with the hurricane occurred. Available at the beginning of our investigation, the pre-event lidar-derived DEMs have formed the topographic mainstay for U.S. Geological Survey studies of these recent landslides. We used these data for calibration and validation of our soil depth and slope stability models. After Hurricane María, the U.S. Geological Survey (2020a, b, c) acquired additional lidar data covering the entire island in 2018. These data, referred to hereafter as post-event lidar, constitute the (currently) best available representation of topographic conditions after the landslides and are useful for assessing susceptibility to future landslides. The 0.5-m post-event lidar DEMs were resampled to 1-m resolution for consistency with the pre-event lidar DEMs and computational efficiency of landslide susceptibility models. We used these post-event DEMs to run our models (using the previously calibrated and evaluated input parameters) to obtain our best estimate of susceptibility to future landslides.

3.2 Engineering data compilation

Based on findings by Bessette-Kirton et al. (2019a) and Hughes and Schulz (2020a, b) indicating strong correlation between landslide density and both bedrock and soil type, Baum (2021) compiled existing data on soil texture and engineering properties to create typical values for model calibration. Four different sources yielded soil and (or) engineering data: (1) published literature about past and recent landslides in Puerto Rico (Sowers 1971; Jibson 1989; Simon et al. 1990; Larsen and Torres-Sanchez 1992, 1998; Lepore et al. 2013; Thomas and Cerovski-Darriau 2019), (2) NRCS soil databases (Soil Survey Staff; 2018), (3) laboratory testing (Smith et al. 2020), and (4) geotechnical reports of recent landslides (Puerto Rico Department of Transportation, written commun. 2019). The NRCS soil data and geotechnical reports were summarized in spreadsheets and then analyzed to determine means, ranges, and other basic statistics to characterize the properties of soils and geologic formations found throughout the three municipalities (Baum and Lewis, 2023). The database compiled from these sources and measured using various protocols, though inhomogeneous, brackets the probable ranges of engineering properties. Baum (2021) identified dominant soil classes of the geologic terranes that had high landslide densities (Fig. 1) and estimated expected ranges of soil strength parameters, cohesion, c', and angle of internal friction, ϕ', both for effective stress based on dominant Unified Soil Classification System (ASTM International, 2020) types in each terrane as follows: volcaniclastic, high-plasticity organic clay (OH), ϕ' 17º – 35º , c' 5 – 20 kPa; submarine basalt and chert, low plasticity clay (CL) and high-plasticity silt (MH), ϕ' 27º – 35º , c' 5 – 20 kPa; granitoid, low plasticity clay (CL) and silty sand (SM), ϕ' 27º – 41º , c' 0 – 20 kPa. Laboratory tests at low normal stress (Smith et al. 2020), relevant to shallow landslides, indicate higher friction

ranges: volcaniclastic, high-plasticity silt (MH) to organic clay (OH), ϕ' 35º – 46º, c' 0 – 5.1 kPa; granitoid silty sand, ϕ' 35º – 54º, c' 0.4 – 4.6 kPa.

3.3 Strength parameter analysis

Using 1D slope stability analysis, Baum (2021) estimated the ranges of soil strength parameters φ' and c' that explain the largest number of field-observed landslide slope and depth combinations in the calibration areas (Fig. 5). Computing 1D factor of safety using the infinite slope analysis (Taylor, 1948; Iverson, 2000), F_1, for 1440 possible incremental combinations of ϕ' and c' over a synthetic grid in which slope angle, δ, and landslide depth, H, varied incrementally over the observed ranges of slope (22° – 60°, in 0.5° increments) and depth (0.2 m – 15 m, in 0.1-m increments) produced F_1 values for more than 1.9×10^7 combinations of H, δ, φ', and c'. The best fitting ranges (dark red in Fig. 6) included combinations of H, δ, ϕ', and c', where more than 75% of observed landslide scarp points were successfully predicted by $F_1 \geq 1$ for $\psi=0$ (dry, where ψ is the pressure head at the basal slip surface) and $F_1 < 1$ for $\psi=H\cos^2\delta$ (water table at the ground surface with slope-parallel flow). The example depicted in Fig. 5 had an overall success rate of 93% for its c' – ϕ' combination (c' = 0.75 kPa and $'$ = 54°) in all three geologic terranes (Figs. 1, 5a). Compiling the performance of every c'-ϕ' pair considered in the analysis led to Fig. 6b, 6c, and 6d, which showed the better-performing ranges of c' and ϕ' for the granitoid (Fig. 6b), volcaniclastic (Fig. 6c), and submarine basalt and chert (Fig. 6d) terranes, respectively. Those combinations of c' and ϕ' with success rates exceeding 75%, were used as inputs for computing F_1 with trial soil-depth maps in subsequent calibration studies to select a single combination of c' and ϕ' for computing F_1 in each terrane.

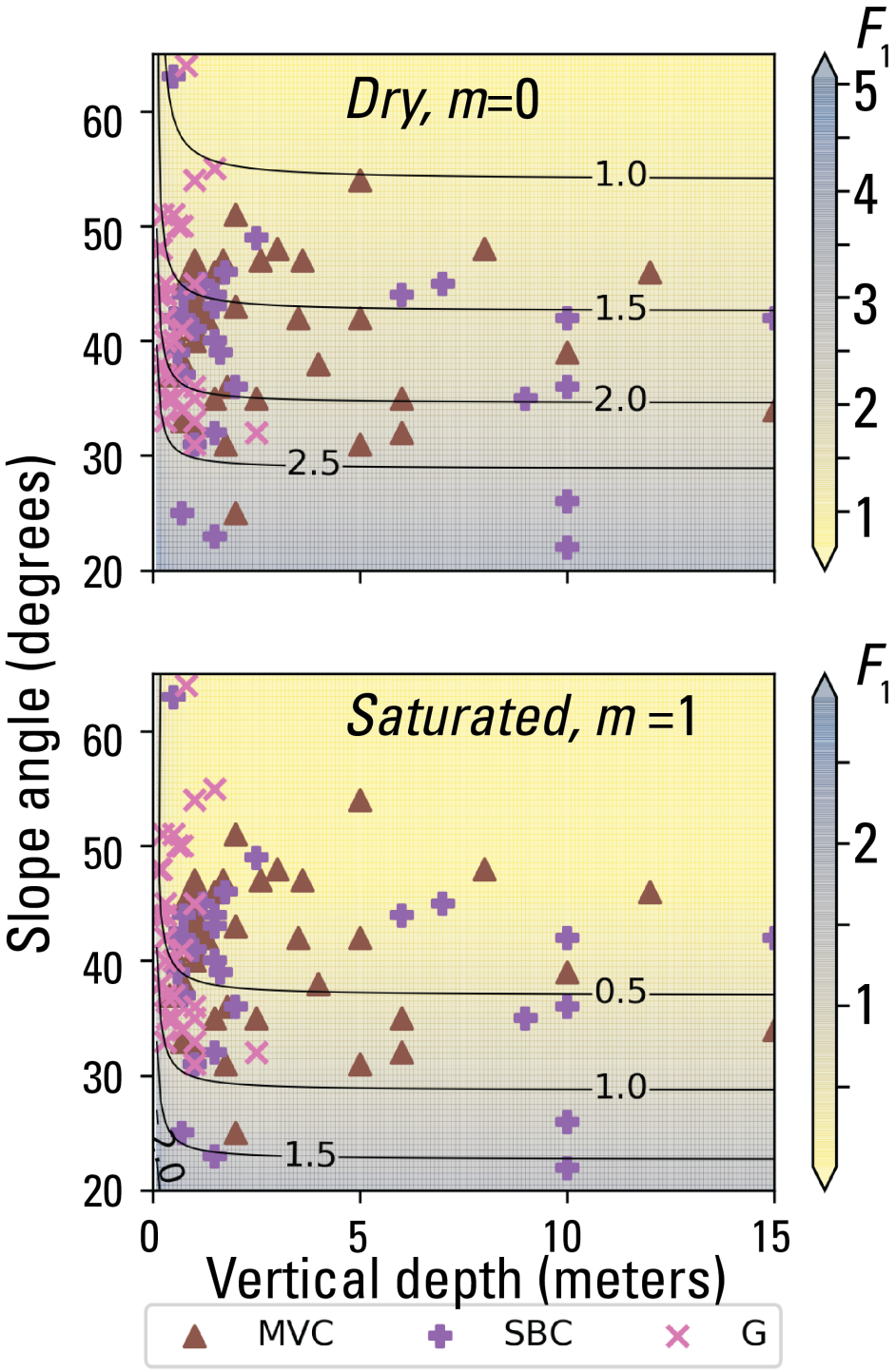

Figure 5. Results of strength parameter testing for observed combinations of landslide slope and depth in three geologic terranes. Factor of safety, F_1, results (indicated by color scale and contour lines) for a selected combination of cohesion, c' (c' = 0.75 kPa) and angle of internal friction, ϕ' (ϕ' = 54°), both for effective stress. Two scenarios for pore-pressure head (m=0 and m=1) are shown, where m is the ratio of pressure head to soil depth. Symbols mark observed slope angle and depth at mapped landslide sources in various geologic terranes (Fig. 1). Factor of safety, F_1, at slope and depth combinations observed at marked landslide sources indicates model success (F_1<1 if m=1) or failure (F_1>1 if m=1). For the pair of c' and ϕ' values shown, F_1>1 for dry conditions (m=0) at about 97% of sources and F_1>1 at 4% of sources for water table at the ground surface with flow parallel to the slope (m=1). These parameters, c' = 0.75 kPa and ϕ' = 54°, had an overall success rate of about 93% (=97% - 4%) for all three terranes (revised from Baum 2021).

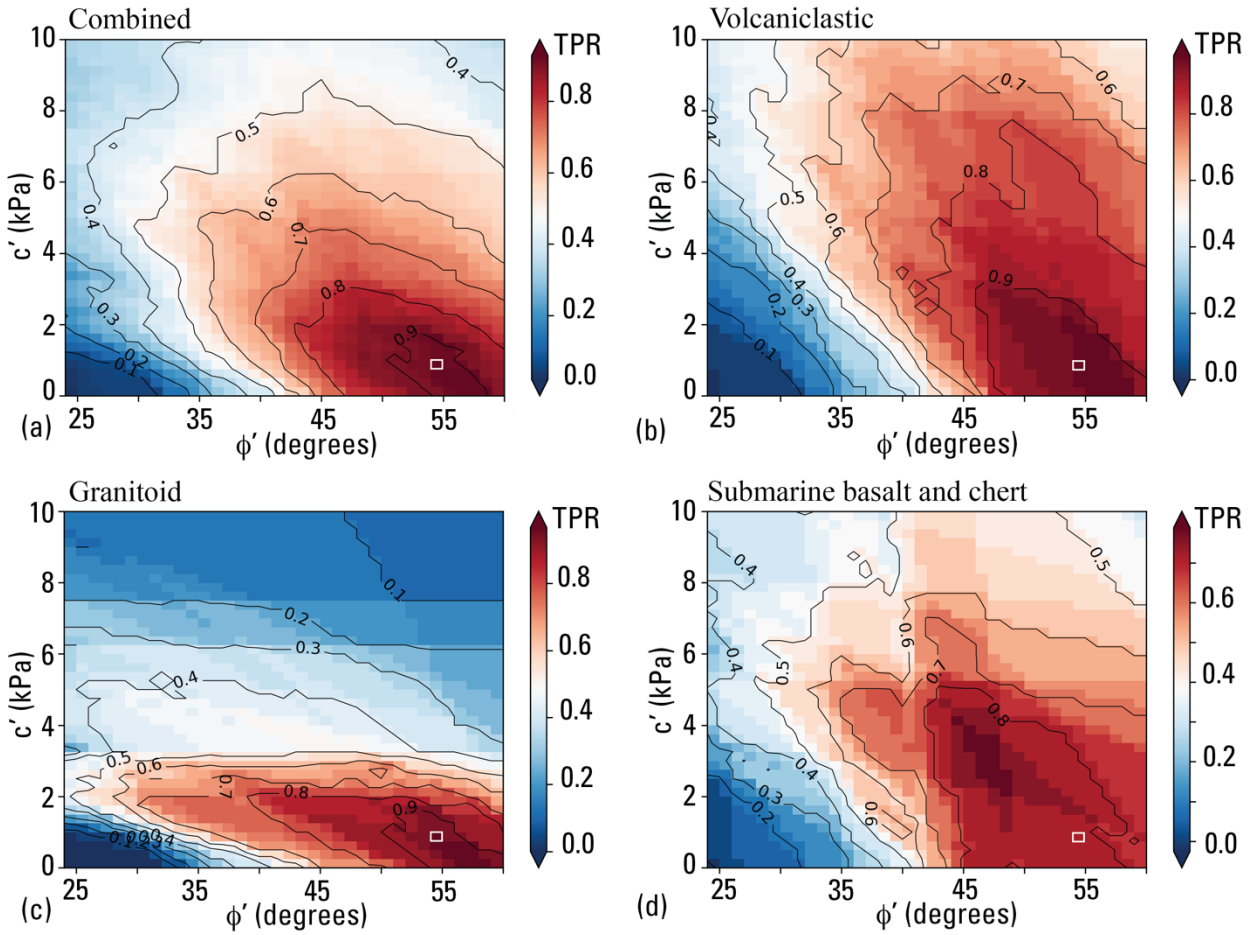

Figure 6. Fraction of field-measured landslide sources from the calibration areas (Baum et al. 2018) predicted correctly as a function of cohesion, c', and angle of internal friction, ϕ', for observed landslides in (a) all three terranes combined (modified from Baum 2021); (b) the volcaniclastic terrane; (c) the granitoid terrane; (d) the submarine basalt and chert terrane. Each pixel summarizes the net result of a pair of analyses like that in Figure 5. Pixel outlined by white rectangle in lower right corner of panels (a), (b), (c), and (d) indicates combination for analysis shown in Figure 5. Pixel color and contours indicate true positive rate (TPR) of predictions for each cell. Factor of safety for dry conditions is $F_{1m=0}$; factor of safety for water table at ground surface with slope-parallel flow is $F_{1m=1}$. Each grid cell represents the fraction $(NF_{1m=0} - NF_{1m=1})/N_t$, where $NF_{1m=0}$ is the number of source areas for $F_1 \geq 1$, $NF_{1m=1}$ is the number of source areas for which $F_1 \geq 1$, and N_t is the number of source areas in the geologic terrane.

3.4 Soil-depth model calibration

Field observations indicated that the base of most landslide sources occurred near the top of weathered bedrock (Baum et al. 2018; Baum 2021), so we chose soil depth as a predictor of landslide source depth. We carried out soil-depth estimation from DEMs using new open-source software, REGOLITH (Baum et al. 2021) containing five empirical and four steady-state process-based soil-depth models implemented in a command-line program. Each model in REGOLITH estimates soil depth from some combination of topographic variables, including slope, upslope contributing area, and curvature, as well as a few model parameters, such as characteristic depth (the soil thickness at which bedrock lowering falls to 1/e of its maximum value), h_0 [L]; critical slope (angle of stability at which the slope

is capable of transporting the entire soil profile by mass movement), δ_c [degrees]; and the ratio of maximum bedrock lowering rate to hillslope diffusivity, R_d. These parameters may vary with conditions that influence soil formation, including bedrock and climate. Predicted soil depth is treated as equivalent to and defines column height, H, in subsequent modelling steps. We modified steady-state process-based models (Pelletier and Rasmussen 2009), which predict soil depth only on convex topography, to estimate soil depths in both concave and convex topography. We used a smoothing algorithm available in REGOLITH to reduce abrupt changes in soil depth that may result from DEM roughness. Further details are available in the online documentation found in the code repository (Baum et al. 2021). Our soil-depth, pressure head, and slope-stability models treated roads, cut slopes and embankments the same as other areas.

Soil-depth model calibration proceeded first by fitting soil-depth models to depth observations followed by checking how the best-fitting models performed as input for computing F_1 to predict landslide locations (see Sect. 3.5). Both calibration and checking made use of pre-event 1-m bare-earth lidar digital elevation models for the four ~2-km^2 calibration areas representing the dominant (three) geologic terranes affected by landslides in the study areas (Fig. 1). Landslides had previously been mapped (Bessette-Kirton et al. 2019c) and characterized (Baum et al. 2018) in these four calibration areas (Sec. 2.2, Fig. 3). Tello (2020) described the soil-depth calibration procedures in detail, including parameter ranges considered in the calibration. We summarize important steps here: Field-measured landslide scars on unmodified hillsides (no obvious cut or fill) served as calibration points for soil depth. Only about 7-8 such scars were available for each calibration area. Tello (2020) adjusted GPS location of each calibration point to the center of its corresponding landslide polygon mapped from imagery by Bessette-Kirton et al. (2019c). A 5-m buffer around each point ensured adequate sampling of model depths to be compared with the field-measured maximum depth. Tello (2020) used a provisional version of the soil-depth code, REGOLITH (Baum et al. 2021), to model trial soil-depth distributions for the calibration areas. Multiple runs to incrementally sample the parameter spaces of several different soil models implemented in REGOLITH produced hundreds of trial soil depth grids for each of the four calibration areas. Soil models tested include a linear area- and slope-dependent model (LASD) (Ho et al. 2012) and modified forms of Pelletier and Rasmussen's (2009) non-linear slope- (NSD), area- and slope- (NASD), and slope- and depth-dependent (NDSD) models. Testing these against the field-measured landslide-scar maximum depths resulted in optimized input parameters for each model and area (Tello 2020).

Tello (2020) used a range of statistical metrics identified by Gupta et al. (2009) to determine predictive success of the model outputs. Most important of these was the Euclidian distance from the ideal point, *ED*. The ideal point is characterized by perfect correlation between observed and simulated points and by perfect agreement between the means and standard deviations of the observed and simulated point distributions,

$$ED = \sqrt{(r-1)^2 + (\alpha-1)^2 + (\beta-1)^2} \quad (1)$$

where the ideal point is at r=1, α=1, β=1 so that ED=0. The linear correlation coefficient, r, relative variability, α, and the bias relative to the observed sample, β, define the ED in eq. (1) (Gupta et al. 2009). In eq. (1) the relative variability is the ratio of the standard deviation of the simulated values, σ_s, to the standard deviation of the observed values, σ_o, (α=σ_s/σ_o). Likewise, the bias is the ratio of mean of the simulated values, μ_s, to the mean of the observed values, μ_o (β=μ_s/μ_o). The linear correlation coefficient, r, indicates the quality of a least-squares fit of the simulated values to the

observed values, with r=1 indicating a perfect fit. The model run having the lowest ED usually had the best fit, unless ED > 1 (Tello 2020). Where ED>1, we chose the model run with β closest to 1 so that the mean simulated depth would be as close as possible to the mean of depth observations (Gupta et al. 2009). The best-fit soil-depth distribution corresponded in turn to a best-fit parameter set for each soil-depth model type. Comparison of best scores for each model type identified the overall best fit of all models tested.

3.5 Soil model evaluation and one-dimensional slope-stability model calibration

To further evaluate the soil-depth modelling results and finish calibrating the slope-stability model, we computed ψ and F_1 as implemented in TRIGRS (Baum et al. 2010; Alvioli and Baum (2016) for dry and steady saturated soil conditions (supplemental text S1 and S2) using the better performing soil-depth models for each calibration area. Previously defined better performing (TPR ≥ 75%) ranges of φ′ (38°-60°) and c' (0-4 kPa) (Baum 2021; Fig. 6b, 6c, 6d) defined the parameter space for computing F_1 with a well-performing subset of trial soil-depth distributions. In addition, we required $F_1 > 1$ in 99.9% of grid cells for ψ(H)=0 to ensure slope stability under dry conditions. Computing F_1 over the calibration areas using the best-fit distributions for each soil-depth model type and ϕ′ and c' combinations produced many F_1 grids. Receiver Operator Characteristics (ROC) analysis (Metz, 1978; Fawcett 2006; Begueria 2006) of these F_1 grids against mapped landslide scarp points indicated which combinations of trial soil-depth distribution and strength parameters predicted the most observed landslides, based on the area under the ROC curve. Using parameters from the highest performing F_1 distribution, we selected the preferred soil depth model and ϕ′ and c' values for modelling F_1 in the large study areas enclosing Lares, Utuado, and Naranjito municipalities. The calibration areas represented different geologic terranes having the highest densities of landslides in the study areas so that the calibration procedure yielded separate model and parameter values relevant to each of these terranes.

3.6 Quasi-three-dimensional slope stability calibration

After H and F_1 values had been improved as much as possible by calibration, we began test calculations of F_3 as implemented in the new open-source code Slabs3D (Baum, 2023; supplemental text S3) and worked to further refine potential landslide source areas. We varied the size of the trial surface from a 3.5-m radius to a 10.5-m radius (Fig. 7) and used ROC analysis along with information about observed source-area sizes to determine the optimum F_3 radius. In addition to these quantitative assessments, we inspected the maps to confirm that the susceptibility zones and potential source areas made sense topographically, mechanically, and geologically. These inspections helped ensure that potential landslide source areas were consistent with observations and expectations for hillsides whether they were relatively undisturbed or modified by roads, cut slopes, and embankments. The inspections led to some minor revisions of the computer code to correct map errors (such as spurious spots of low factor of safety), followed by repeated model runs.

Due to insufficient data, rigorous calibration was not possible for some areas, such as the karst areas of Bawiec's (1998) Limey sediment terrane. We adjusted model parameters (reduced maximum soil depth, H_{max}, and characteristic soil depth, h_0, for the soil-depth model and increased c' for computing F_1 and F_3) for the Limey sediment terrane to account for the terrane's low landslide density during Hurricane María.

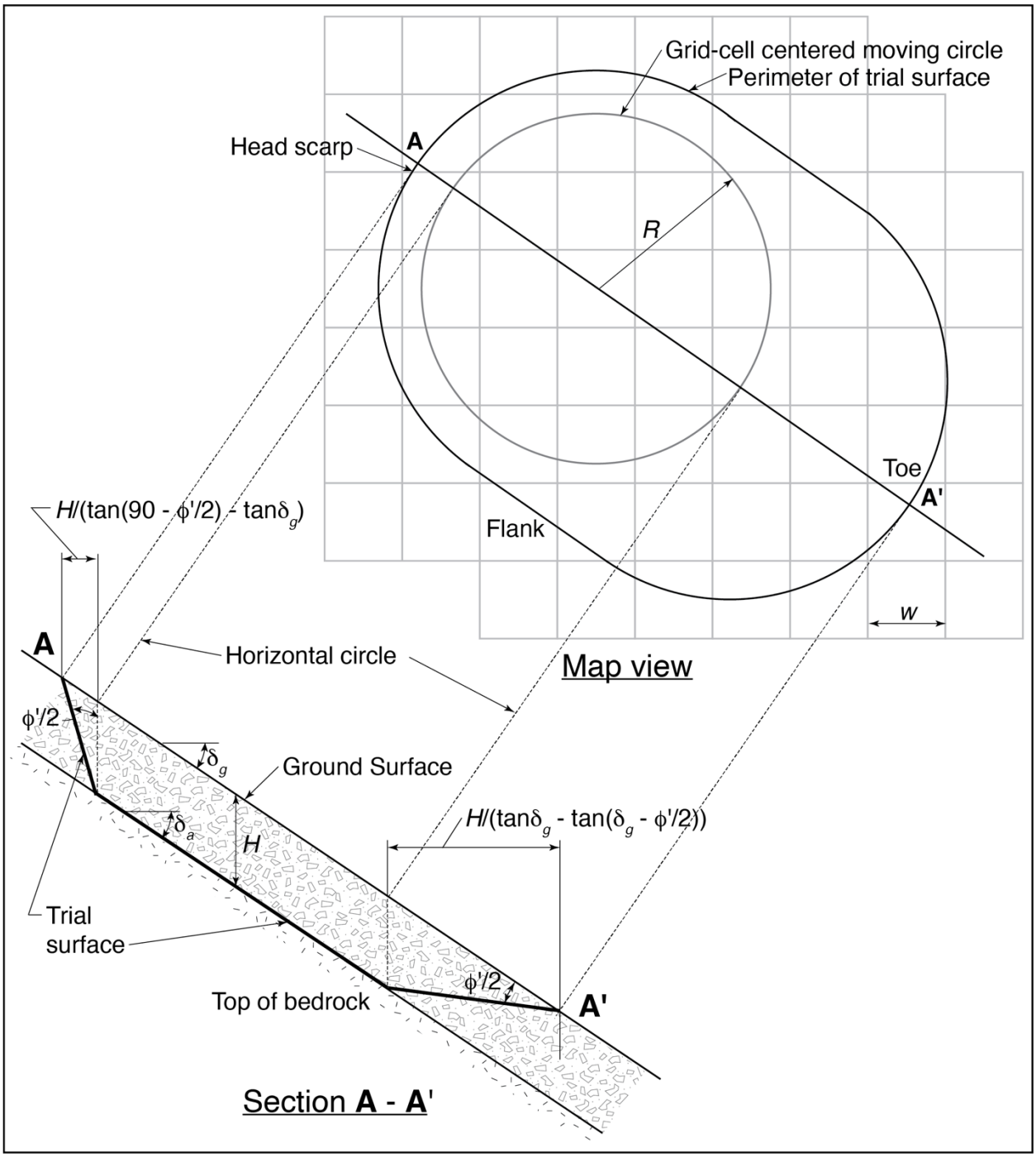

Figure 7. Sketch showing moving circle search strategy and trial surface geometry used in computing approximate 3D factor of safety, F_3. All grid cells whose center is inside the circle are included in the computation of F_3, and cells in the head scarp, flank, and toe areas are combined to form wedges for computational purposes. The trial surface has a map-view radius R; δ_g is the slope of the ground surface; δ_a is the apparent dip of the trial surface in the assumed direction of sliding (average slope direction of grid cells centered within the horizontal circle); H is height of a grid-cell centered column from the trial surface to the ground surface; and ϕ' is the angle of internal friction of the soil for effective stress (modified from Baum et al. 2012). For the case depicted in Section A-A′ (above), H is constant and 1.5 times the horizontal width, w, of the square grid cells. As the average value of H/w decreases and as R increases, the perimeter of the trial surface contracts toward the projection of the horizontal circle onto the ground surface. For variable soil-depth models, H may vary from cell to cell and the value of H for the grid cell closest to the upslope or downslope edge of the horizontal circle is used in the formulas shown in the cross section for horizontal dimensions of the scarp and toe respectively.

3.7 Geologic mapping and parameter zonation

Bawiec (1998) compiled published 1:20,000-scale geologic mapping of Puerto Rico and (as noted previously) combined related formations into geologic terranes (Fig. 1 and Bawiec 1998). Based on the results of early studies (Bessette-Kirton et al. 2019a) and our calibration efforts, the geologic terranes became the basis for subdividing the study areas into parameter zones. The topographic base maps available at the time of geologic mapping lacked the detail of the pre-event lidar-derived topography used in this study. Trial computations of F_1 and F_3 on the study area DEM tiles indicated that a uniform soil depth model across the highly susceptible geologic terranes resulted in a more accurate susceptibility map than a zoned model using the calibrated soil-depth parameters. This was likely a consequence of (1) having few soil-depth observations available from unmodified hillsides in each zone (section 3.4) as well as (2) a high degree of land surface modification from past agricultural activities, and road and residential construction resulting in weak calibration of the volcaniclastic and submarine basalt and chert geologic terranes. Consistent with results in Fig. 6a, uniform values of ϕ' and c' for the highly susceptible geologic terranes likewise resulted in good performance so we used the same soil depth and strength parameters for all three terranes (Supplemental Figures S1 and S2). Consequently, slight uncertainty in locations of boundaries between these terranes had no effect on computed F_1 and F_3 values. However, a large difference in landslide susceptibility and model parameters (maximum soil depth, h_0, c') existed between the Limey sediment terrane with its cone karst and the highly susceptible terranes of the basement complex (submarine basalt, volcaniclastic, and granitoid). Offsets as great as tens of meters in the contact between the Limey sediment terrane and its neighbors along a prominent escarpment in Lares and Utuado resulted in errors in F_1 and F_3 along the escarpment. Consequently, Perkins et al. (2022) remapped the Limey sediment contact using lidar-derived shaded relief images and optical imagery to accurately delineate the transition from high to low landslide susceptibility across the contact. The contact was discerned based on the visually distinct differences between the closed basins and rugged karst cones of the Limey sediment terrane and the steep ridges and narrow branching valleys of the basement rocks.

3.8 Soil-depth modelling

After completing the calibration process, we created the overlapping rectangular tiles (described previously, Sec. 1.0, 3.1) from the pre-event lidar bare-earth DEMs (Fig. 4, stage C and Fig. 1b, 1c). We created additional input files from the lidar-derived DEM tiles: flow accumulation grids for use with the area-dependent soil-depth models and parameter-zone grids for specifying different model input parameters (Sec. 3.6, 3.7, Fig. 4). The parameter zones ensured a thinner and less continuous modeled soil mantle in the karst (Limey sediment terrane) than in areas underlain by the landslide-prone geologic terranes (Fig. 1). For comparison with the soil-depth models, we also used constant soil depth equal to the average depth, 1.4 m, observed at landslide scars.

3.9 Pressure-head and slope-stability modelling

Raster grids created from the soil-depth modelling defined soil depth (H) and slope of the ground surface at each grid cell. We computed ψ and F_1 using TRIGRS (Baum et al. 2010; Alvioli and Baum 2016), version 2.1, using the same lidar-derived DEM tiles and parameter zones as for soil-depth modelling (Fig. 4). Then, using $\psi(H)$ computed with

TRIGRS (supplemental text S1) along with the same lidar tiles, parameter zones, and ϕ' and c' values used in computing F_1 as input for Slabs3D, we computed F_3 (Fig. 4). The radius of each trial surface, as constrained by earlier testing in the calibration areas (Sect. 3.6, 4.5), was held constant at 3.5 m for all model runs on study area tiles.

3.10 Model testing and evaluation

We used ROC analysis of F_3 grids based on pre-event lidar topographic data compared to landslide head-scarp points mapped by Hughes et al. (2019) as a basis for testing performance and then defining susceptibility categories (Fig. 4). Selecting the minimum F_3 value within a 3-m radius around the scarp points accounted for uncertainty in their mapped locations. Validating F_3 for pre-event topography was appropriate because it most accurately portrayed conditions at the time of Hurricane María. We computed true positive rate (TPR), false positive rate (FPR), and area under the TPR-FPR curve (AUC) and distance to perfect classification, D2PC, (0,1), (Formetta et al. 2016) to evaluate performance of pre-event F_3 as a predictor of observed landslide scarp points. Analyzing landslide density distribution across F_3 provided a further check on model accuracy. We computed landslide densities in 0.1 increments of F_3 to check for a general trend of decreasing observed density with increasing F_3. We also continued map inspections as described in Section 3.6.

As an additional check we computed ROC statistics for minimum F_3 values within source areas mapped by Baxstrom et al. (2021a) and Einbund et al. (2021a, 2021b). Their detailed landslide source mapping covers only a fraction of the study areas (Fig. 1), whereas the scarp points mapped by Hughes et al. (2019) cover the entire island. However, source area polygons enclose pixels that are more relevant to testing performance of F_3 than circles centered at the scarp points.

Evaluating the model to address the need for a conservative landslide susceptibility map led us to select threshold values of F_3 enclosing specific percentages (or TPR) of landslide points. Our reason for doing so rather than placing the category break at $F_3 = 1$ is to account for model and parameter uncertainty. Every F_3 contour on the map encloses a specific percentage of landslide points. Contours at high F_3 values enclose more landslide points than low F_3 contours. We selected F_3 contours corresponding to TPR of 0.75 and 0.90 of Hurricane María-produced landslide head-scarp points (Hughes et al. 2019) to define the limits of very high (TPR $\leq$ 0.75), high (0.75 $\leq$ TPR $\leq$ 0.90), and moderate (TPR > 0.90) landslide source susceptibility zones. The high and very high susceptibility zones both indicate significant danger from landslides but allow users to distinguish areas having greater potential for long runout (Brien et al. 2021). These classes include most mapped landslide points as well as the adjacent steep slopes where they occurred, while limiting the overall areal extent of the very high and high susceptibility classes.

3.11 Modelling potential landslides on post-storm topography

After modelling potential source areas on pre-event topography, we recomputed the soil depth, pressure head, and factor of safety using post-event 1-m lidar topography (U.S. Geological Survey, 2020a, b, c). We generated new slope, zone, and flow-accumulation grids from the post-event lidar and then ran REGOLITH, TRIGRS, and Slabs3D in succession (Fig. 4) to indicate our best estimate of susceptibility to future landslide initiation.

3.12 Removing edge effects and applying susceptibility categories

We joined the four overlapping tiles for Lares and Utuado to create a final landslide susceptibility map (based on post-event lidar). To reduce edge effects (Fig. 4) when joining the four tiles, we first removed a 100-m buffer along all edges of each tile. At grid cells where two tiles overlapped, differences in F_3 tended to be small and we retained the greater F_3 value. For the single tile covering Naranjito, we removed only the 100-m buffer along all tile edges.

We then classified landslide susceptibility for post-event topography across the three municipalities using the same F_3 thresholds at TPR ≤ 0.75 and TPR ≤ 0.90 determined for the pre-event topography (Fig. 4). These thresholds divide the map area into zones of varying susceptibility to landslide initiation. The resulting susceptibility zones estimate the potential for future shallow landslides (Fig. S1 and S2).

4 Results

4.1 Soil-depth calibration

We calibrated soil depth to field measurements (Fig. 4, section 3.4) for three (ANA, LAR, UTU) of the four calibration areas and calculated Euclidian distance from the ideal point, ED (Eq. 1), correlation coefficient, r (and other statistical parameters as outlined in Tello 2020) to determine which models and parameter sets gave the closest match to field observations (Fig. 8a, b). No soil depth calibration was performed for NAR as depth measurements in Naranjito were mainly outside the area mapped by Bessette-Kirton et al. (2019c). Limiting the observed depths to landslide scars on relatively unmodified slopes resulted in sample sizes of only seven or eight observation points (landslide sources) per calibration area. Most soil-depth models for the Utuado calibration area (UTU) had acceptable performance as indicated by positive correlation between observed and simulated depths ($0.08 \leq r \leq 0.78$), and ED ranging from 0.28 to 0.99 (Fig. 8a; Tello 2020). Of these, the modified nonlinear area and slope (NASD) model had the smallest ED, 0.28, and the largest r, 0.78 (Fig. 8a). Other better-performing models were a nonlinear slope-dependent model with linear area dependance (NSDA) and a linear area- and slope-dependent model (LASD) based on the wetness index (Ho et al. 2012). In contrast, most soil-depth models for the Añasco (ANA) and Lares (LAR) calibration areas performed poorly, with negative or small positive correlation ($r < 0.16$) and $0.69 < ED < 1.8$ (Fig. 8a). The poor correlation probably resulted from the small sample sizes of observed depths in these areas. At LAR, only the nonlinear slope dependent model (NSD, see Pelletier and Rasmussen 2009) had acceptable performance with r = 0.78 and ED=0.69 (Fig. 8a). The NASD model had α and β closest to 1, for both ANA and LAR (Fig. 8b).

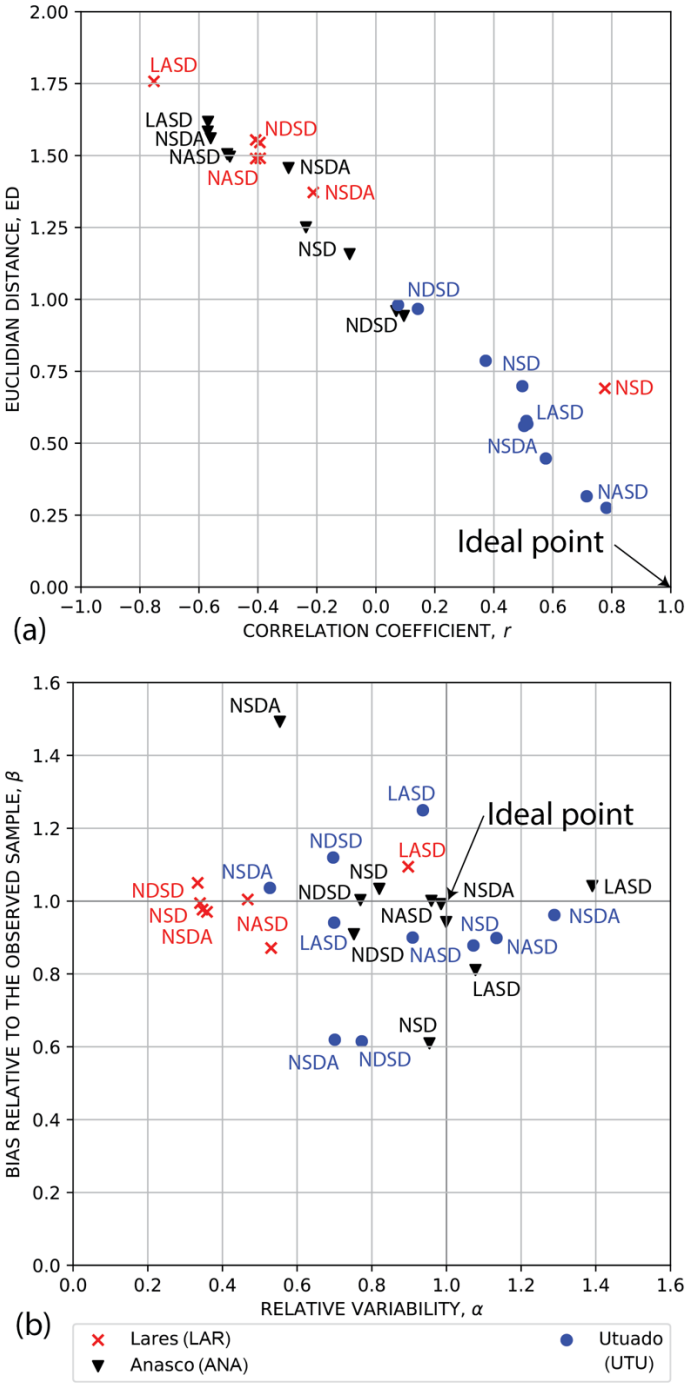

Figure 8. Soil-depth model calibration measures for Anasco (ANA), Lares (LAR) and Utuado (UTU) calibration areas (Fig. 1). Performance is based on comparing maximum landslide depth at field-mapped landslide points from unmodified hillsides against modeled depths within a 5-m radius of the point for all field-mapped points in the calibration area. GPS point locations were corrected as needed by moving them to the centers of corresponding landslide polygons mapped by Bessette-Kirton et al. (2019c). (a) Primary metrics, Euclidian distance from the ideal point, ED (smaller is better), versus correlation coefficient, *r*, (b) bias relative to the observed sample, β, versus relative variability, α. The ideal point is at *r*=1, α=1, β=1. [Soil-depth models: LASD, linear area- and slope-dependent model; NASD, nonlinear area- and slope-dependent model; NDSD, nonlinear depth- and slope-dependent model; NSD, nonlinear slope-dependent model; NSDA, nonlinear slope-dependent model with linear area dependence].

4.2 Soil-depth model evaluation and slope-stability calibration results

Slope stability parameter calibration compared F_1 values for previously determined ranges of c' and ϕ' (Fig. 6) for each of the soil depth models to find the best-performing combination of soil model and strength parameters for predicting landslide source locations in each calibration area (Fig. 4, section 3.5). For UTU, the NASD model performed best with the NSDA model close behind (Tello 2020) based on area under the TPR – FPR curve and minimum distance of the curve from the perfect classification. Parameter combinations and ROC results for the best-performing model in each area appear in Table 1. Despite poor soil depth model performance metrics for ANA and LAR (Fig. 8), the F_1 calculations for the three calibration areas indicated that the NASD soil depth model had the greatest predictive strength for locations of landslide source areas in ANA, LAR, and UTU with similar results (Table 1). Despite lack of soil-depth calibration in NAR, results in this study area were like the other three calibration areas (Table 1). Values of δ_c near 60° gave the best soil-depth model results (Table 1), despite variability in the steepest slopes where landslides occurred in the different terranes (Fig. 3d, 4).

Table 1. Calibration results for 1D factor of safety, F_1, with soil depth models by calibration area (Fig. 1). Positives and negatives in the ROC analysis based on total pixels within and outside the estimated source areas of landslide polygons mapped by Bessette-Kirton et al. (2019c) and whether the pixels have F_1>1 or F_1<1 (Tello 2020). [Symbols and abbreviations: NASD, non-linear area and slope dependent soil-depth model of Pelletier and Rasmussen (2009) as modified by Baum et al. (2021); H_{max}, maximum soil depth; δ_c, critical slope angle; R_d, diffusivity ratio; c', soil cohesion for effective stress; ϕ', angle of internal friction for effective stress; AUC, area under the curve of true-positive-rate (TPR) and false positive rate (FPR) (larger is better); D2PC, distance from the perfect classification, (0,1), to nearest point on the TPR-FPR curve (smaller is better); Best F_1, 1D factor of safety at point on the TPR-FPR curve nearest to the ideal point, (0,1), and therefore the most accurate F_1 classifier of landslide versus non-landslide grid cells for the particular model (closer to one is better); °, degrees.]

Calibration area	Soil Model	H_{max} (m)	δ_c (°)	R_d	c' (kPa)	ϕ' (°)	AUC	D2PC	Best F_1
Utuado (UTU)	NASD	2.0	60	1.0	2.5	45°	0.67	0.48	1.5
Añasco (ANA)	NASD	3.0	60	0.16	4.5	45°	0.70	0.46	1.1
Lares (LAR)	NASD	3.0	60	0.25	4.5	45°	0.66	0.52	1.1
Naranjito (NAR)	NASD	3.0	60	0.2	4.0	45°	0.65	0.54	1.2

4.3 Modeled soil depth

Having completed the soil-depth model calibration (Sec. 4.1) and testing (Sec. 4.2), we modeled soil depth in the larger map tiles preparatory to analyzing slope stability (Fig. 4, section 3.8). Each tile covers hundreds of km^2, so we illustrate results using the NAR area, chosen to demonstrate that our susceptibility workflow can achieve very good results even with limited landslide source depth observations. As noted previously, insufficient field-measured landslide points prevented soil-depth model calibration (Sec. 4.1), but not model evaluation and slope stability

calibration (Sec. 4.2) for NAR. Figure 9 shows predicted soil depth for the best performing soil-depth model (based on the slope-stability evaluations, Sec. 4.2) in NAR (see Fig. 1 for location). The model shown in Fig. 9 predicts greater soil depth in hollows than on ridges. Other models that were tested (not shown) produced somewhat similar results. Differences in model structure produce different responses to topographic features, including flat areas, road cuts, and steep slopes. For example, the modified NASD and NSDA models predicted deep soils (≤3 m for parameters chosen) in convergent areas, on steep slopes, including road cuts and embankments; thin soils on ridge crests, and thin or no soil on downslope flat areas (see large flat area on east edge of Fig. 9). In contrast, the LASD and NDSD models predicted deep soils (≤3 m for parameters chosen) in convergent areas and on flats and thin soils on ridge crests and steep slopes (except where they occur in strongly convergent topography). These topographic features were more distinct in the three nonlinear models, NASD, NSDA, and NDSD, than in the linear LASD model.

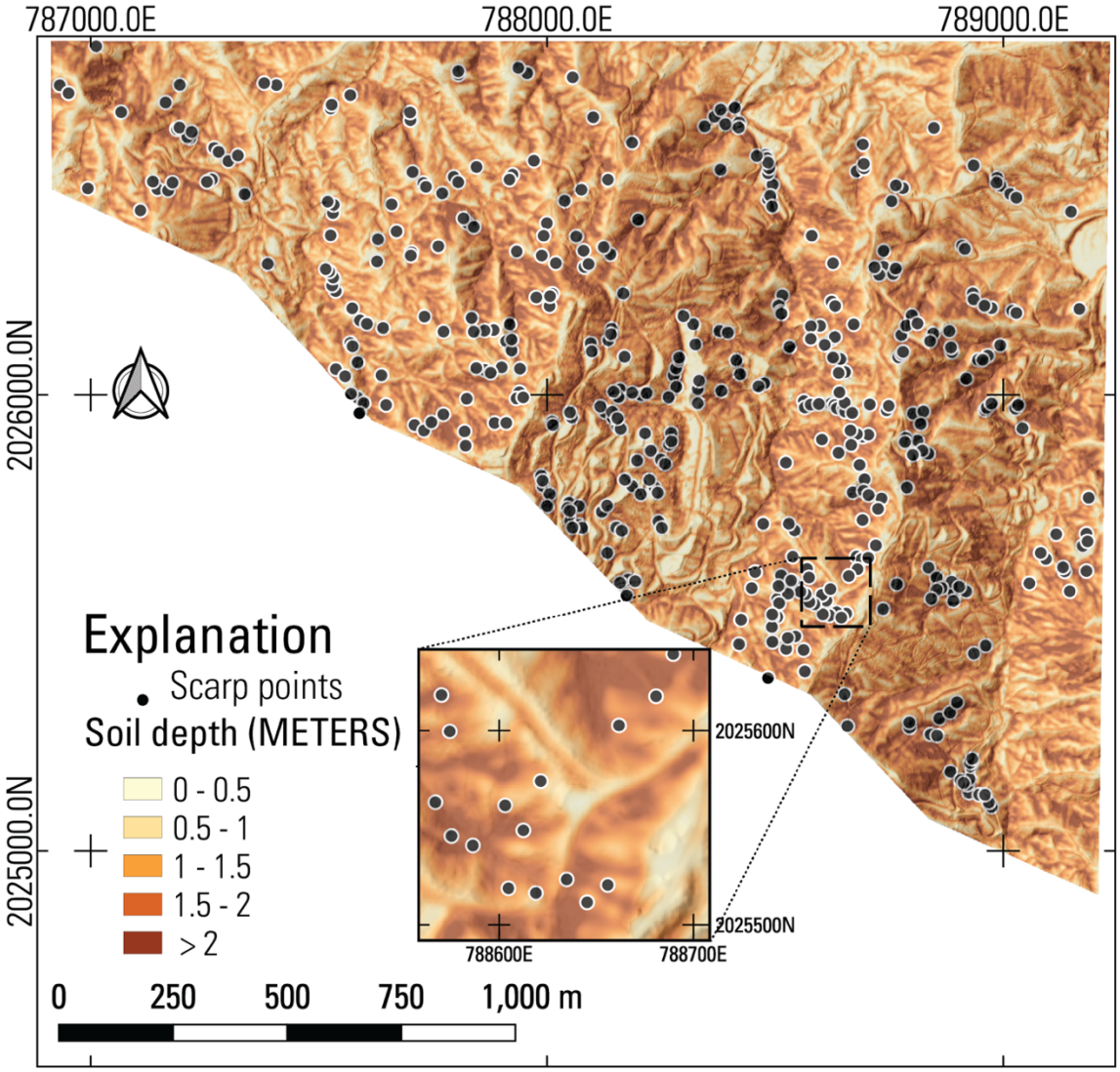

Figure 9. Best-performing version of soil depth maps from soil-depth models tested for the Naranjito (NAR) calibration area in volcaniclastic terrane (Fig. 1). Topographic base derived from lidar by U.S. Geological Survey (2018), scarp points from Bessette-Kirton et al. (2019c). The modified Nonlinear Area- and Slope-dependent (NASD) model (modified from Pelletier and Rasmussen 2009, as implemented by Baum et al. 2021) depicted here, was the overall best-fitting soil-depth model for this terrane. Inset shows details of a 150 m by 150 m area, with thicker soil accumulation in concave areas.

585 **4.4 One-dimensional factor of safety**

586 Figure 10 shows F_1 optimized for NAR and calculated using TRIGRS and the soil model results in Fig. 9, as well as
587 F_1 for constant soil depth. Slopes steeper than 60°, the estimated critical slope angle, were treated as barren (zero or
588 negligible soil thickness) and stable because landslides were very rare on slopes steeper than 60° (Fig. 3d). On slopes
589 flatter than 60°, soil strength parameters are within the ranges obtained by sensitivity analysis of F_1 parameters ϕ' and
590 c' over observed ranges of slope and depth of landslides characterized in the field at ANA, LAR, UTU, and NAR (Fig.
591 6). The only landslide source locations available throughout the three municipalities are the scarp points of Hughes et
592 al. (2019). Due to location uncertainty, we used a 3-m radius around the scarp points for defining true positives. Color
593 thresholds on the maps (Fig. 10) are based on F_1 at TPR of 0.75, 0.90, and 0.95. Consequently, thresholds for F_1 differ
594 for each panel in Fig. 10. The same TPR values (0.75, 0.90, 0.95) were used for picking F_3 thresholds for landslide
595 initiation susceptibility across the entire study area covering Naranjito, Utuado, and Lares Municipalities in the final
596 maps (Supplemental Figures S1 and S2).

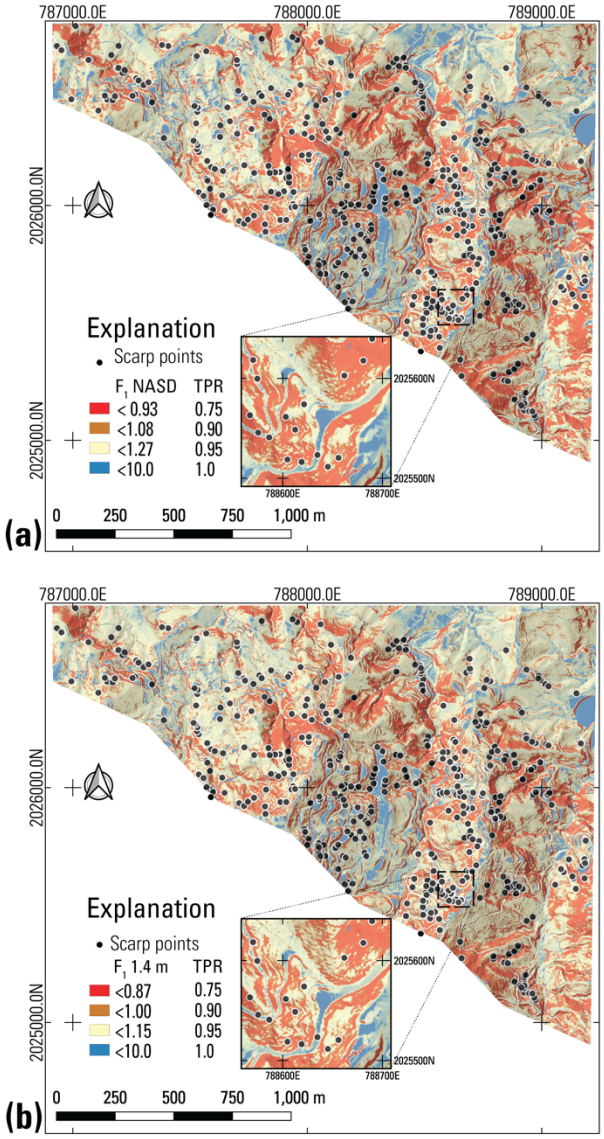

Figure 10. Maps of Naranjito (NAR) calibration area in volcaniclastic terrane (Fig. 1) showing 1D factor of safety (F_1) results for a) soil-depth model shown in Figure 9 as well as b) constant average soil depth. Topographic base derived from lidar by U.S. Geological Survey (2018), scarp points from Bessette-Kirton et al. (2019c). True positives determined by minimum F_1 within a 3-m radius of the scarp points. (a) F_1 for NASD, the modified nonlinear area- and slope-dependent soil-depth model depicted in Fig. 9, (b) F_1 for constant soil depth of 1.4 m. Inset shows details of a 150 m by 150 m area.

Areas of low F_1 are similar in overall pattern between the two maps shown in Fig. 10 but differ in detail. These details include small areas of low F_1 unique to each model as well as variation in the extent of major areas of low F_1. Many boundaries of the areas of low F_1 are ragged and small patches of yellow, indicating higher F_1, occur within the larger red and orange areas of low F_1. Differences in F_1 between the maps are attributable mainly to variation in soil depth and partly to variation in c'. The optimum value of c' varied depending on the characteristics of each soil model (Table 2). The results shown in Fig. 10 are for the best-performing combination of c' and ϕ' for the soil-depth model at NAR (Fig. 9 and Sec. 4.2) and for constant average depth of 1.4 m.

The different F_1 patterns shown in Fig. 10 correspond to slightly different levels of predictive success. The AUC and distance from the perfect classification (0,1) to the nearest point on the TPR-FPR curve, D2PC indicate that F_1 for constant depth has the highest predictive skill (AUC=0.88, D2PC=0.26, F_1 value nearest the perfect classification, F_1=0.9). Next, F_1 for the NASD model performed almost as well (AUC=0.86, D2PC=0.30, F_1 value nearest the perfect classification, F_1=1.0). When applied to the entire DEM tile covering Naranjito municipality, F_1 for constant depth and NASD tied with AUC = 0.86 and D2PC = 0.30 (constant depth) and D2PC = 0.29 (NASD). Thus, the performance edge of constant depth is localized at NAR and does not extend across the entire Naranjito DEM tile. Other soil-depth models performed slightly worse (Table 2) consistent with results obtained by Tello (2020) for UTU. The slightly higher performance for F_1 with constant depth at NAR comes at the cost of the area classified as very high, high, or moderate susceptibility (TPR = 0.95) being more diffuse, with more ragged boundaries, than for F_1 with NASD (Fig. 10a, b). Varying the amount of cohesion used with a particular soil model caused small changes in the AUC, D2PC, and best F_1 as shown by the two entries for NDSD in Table 2.

Table 2. Key inputs and performance measures for factor of safety calculations based on the infinite slope model (F_1), as implemented by TRIGRS, in the Naranjito calibration area (NAR). Performance is based on minimum F_1 within a 3-m radius of landslide scarp points mapped by Hughes et al. (2019). [Symbols and abbreviations: NASD, non-linear area and slope dependent soil-depth model of Pelletier and Rasmussen (2009) as modified by Baum et al. (2021); NSDA, non-linear slope dependent model of Pelletier and Rasmussen (2009) modified by Baum et al. (2021) to include linear area dependence; NDSD, non-linear slope and depth dependent model of Pelletier and Rasmussen (2009); LASD, linear area and slope dependent model of Ho et al. (2012); H_{max}, maximum soil depth; δ_c, critical slope angle; R_d, diffusivity ratio; C_0, empirical constant used in LASD; c', soil cohesion for effective stress; ϕ', angle of internal friction for effective stress; AUC, area under the curve of true-positive-rate (TPR) and false positive rate (FPR) (higher is better); D2PC, distance from the perfect classification, (0,1), to nearest point on the TPR-FPR curve (smaller is better); Best F_1, 1D factor of safety at point nearest to the perfect classification, (0,1), and therefore the most accurate F_1 classifier of landslide versus non-landslide grid cells for the particular model (closer to 1.0 is better); °, degrees ; -- not applicable.]

Soil Model	H_{max} (m)	δ_c (°)	R_d or C_0	c' (kPa)	ϕ' (°)	AUC	D2PC	Best F_1	TPR at D2PC
NASD	3.0	60	0.20	4.0	45°	0.86	0.30	1.0	0.82
LASD	3.0	60	0.45	3.5	45°	0.85	0.31	1.1	0.84
NDSD	3.0	60	0.10	4.5	45°	0.82	0.36	1.2	0.75
NDSD	3.0	60	0.10	2.5	45°	0.86	0.32	1.0	0.89
NSDA	3.0	60	0.10	4.5	45°	0.85	0.30	1.1	0.80
Constant	1.4	60	--	4.0	45°	0.88	0.26	0.9	0.79

4.5 Quasi-three-dimensional factor of safety

Figure 11 shows F_3 computed using the soil-depth model in Fig. 9 and constant soil depth of 1.4 m. Predictive skill for F_3 is somewhat less than F_1; AUC is 0.05 – 0.08 less for F_3 than corresponding F_1 (Tables 2 and 3). The only exception is for the constant soil depth model results where F_3 has the highest AUC, 0.94, of all cases tested (Fig. 12a and 12b). Despite the overall slightly worse performance of F_3 it provided smoother boundaries on the landslide susceptible areas (Fig. 11a, b), which also are more continuous than corresponding F_1 landslide susceptible areas (Fig. 10). The lower AUC values resulted from the F_3 susceptible areas covering slightly more land area than the

corresponding F_1 areas at the same TPR. Therefore, the F_3 susceptibility maps are more conservative than their F_1 counterparts.

Table 3. Key inputs and performance measures for factor of safety calculations based on a quasi-3D limit-equilibrium slope stability model (F_3) in the Naranjito calibration area (NAR). Performance is based on minimum F_3 within a 3-m radius of landslide scarp points mapped by Hughes et al. (2019). [Symbols and abbreviations: NASD, non-linear area and slope dependent soil-depth model of Pelletier and Rasmussen (2009) as modified by Baum et al. (2021); NSDA, non-linear slope dependent model of Pelletier and Rasmussen (2009) modified by Baum et al. (2021) to include linear area dependence; NDSD, non-linear slope and depth dependent model of Pelletier and Rasmussen (2009); LASD, linear area and slope dependent model of Ho et al. (2012); H_{max}, maximum soil depth; δ_c, critical slope angle; R_d, diffusivity ratio; C_0, empirical constant used in LASD; c', soil cohesion for effective stress; ϕ', angle of internal friction for effective stress; AUC, area under the curve of true-positive-rate (TPR) and false positive rate (FPR); D2PC, distance from the perfect classification, (0,1), to nearest point on the TPR-FPR curve; Best F_3, 3D factor of safety at point nearest to the perfect classification, (0,1), and therefore the most accurate F_1 classifier of landslide versus non-landslide grid cells for the particular model (closer to 1.0 is better); °, degrees.]

Soil Model	H_{max} (m)	δ_c (°)	R_d or C_0	c' (kPa)	ϕ' (°)	Trial surface radius (m)	AUC	D2PC	Best F_3	TPR at D2PC
NASD	3.0	60	0.20	0.5	45°	3.5	0.80	0.38	0.9	0.86
NASD	3.0	60	0.20	0.5	45°	6.5	0.75	0.45	0.9	0.66
NASD	3.0	60	0.20	0.5	45°	9.5	0.71	0.50	1.0	0.86
LASD	3.0	60	0.45	0.5	45°	3.5	0.78	0.44	1.0	0.89
NDSD	3.0	60	0.10	0.5	45°	3.5	0.78	0.40	0.9	0.71
NSDA	3.0	60	0.10	0.5	45°	3.5	0.80	0.37	0.9	0.78
Constant	1.4	60	--	0.5	45°	3.5	0.92	0.23	1.0	0.94

Tests indicated that trial surfaces having a map-view radius of 3.5 m provided more accurate estimates of susceptible areas than larger trial surfaces (6.5-m and 9.5-m radius). Other things being equal, larger trial surfaces resulted in smaller AUC and larger D2PC (Table 3, Fig. 12b). The larger trial surfaces tended to widen the susceptible areas and smooth their boundaries, with the result that a larger percentage of the calibration area was classified as susceptible (9.5-m radius, 85%; 6.5-m radius, 83%; 3-m radius, 78% for examples in Table 3). In addition, the 3.5-m radius produced a trial surface close in size (7.5 – 7.9 m wide, with an area of 46 – 48 m^2 at the ground surface for 1-m depth on 30° – 40° slopes) to the median horizontal areas of landslide sources mapped in NAR, 51 m^2, in UTU2, 42 m^2, and in LAR2 64 m^2 (Fig. 3c).

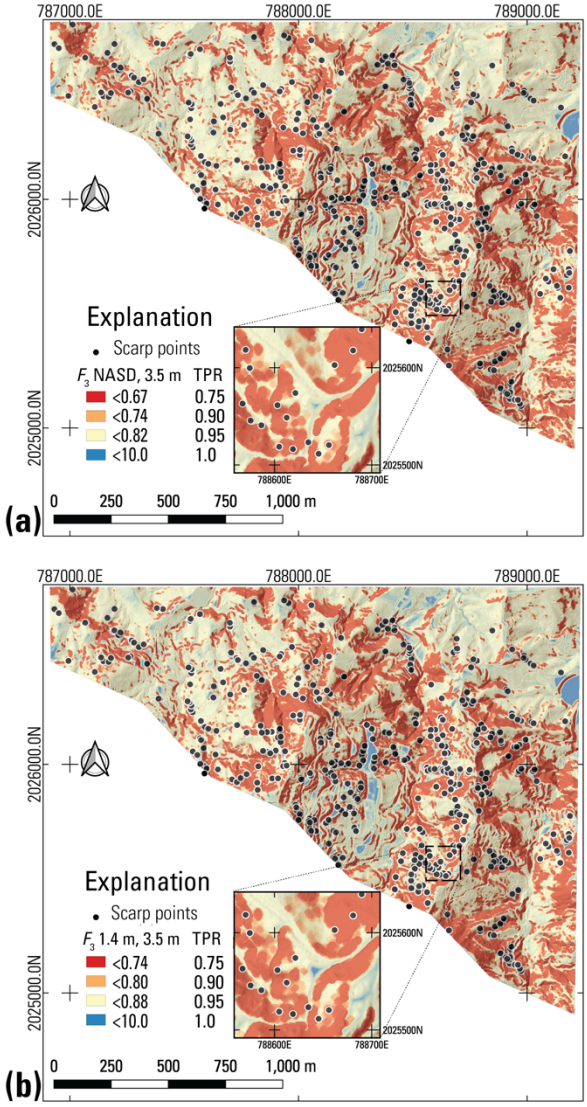

Figure 11. Maps of Naranjito (NAR) calibration area in volcaniclastic terrane (Fig. 1) showing quasi-3D factor of safety, F_3, results for the soil depth models shown in Figure 9. (a) F_3 for the modified nonlinear area and slope dependent (NASD) soil-depth model depicted in Fig. 9, (b) F_3 for constant soil depth of 1.4 m. Inset shows details of a 150 m by 150 m area. The calculation of F_3 used a trial surface of 3.5-m map-view radius (Fig. 7). Topographic base derived from lidar by U.S. Geological Survey (2018), scarp points from Bessette-Kirton et al. (2019c).

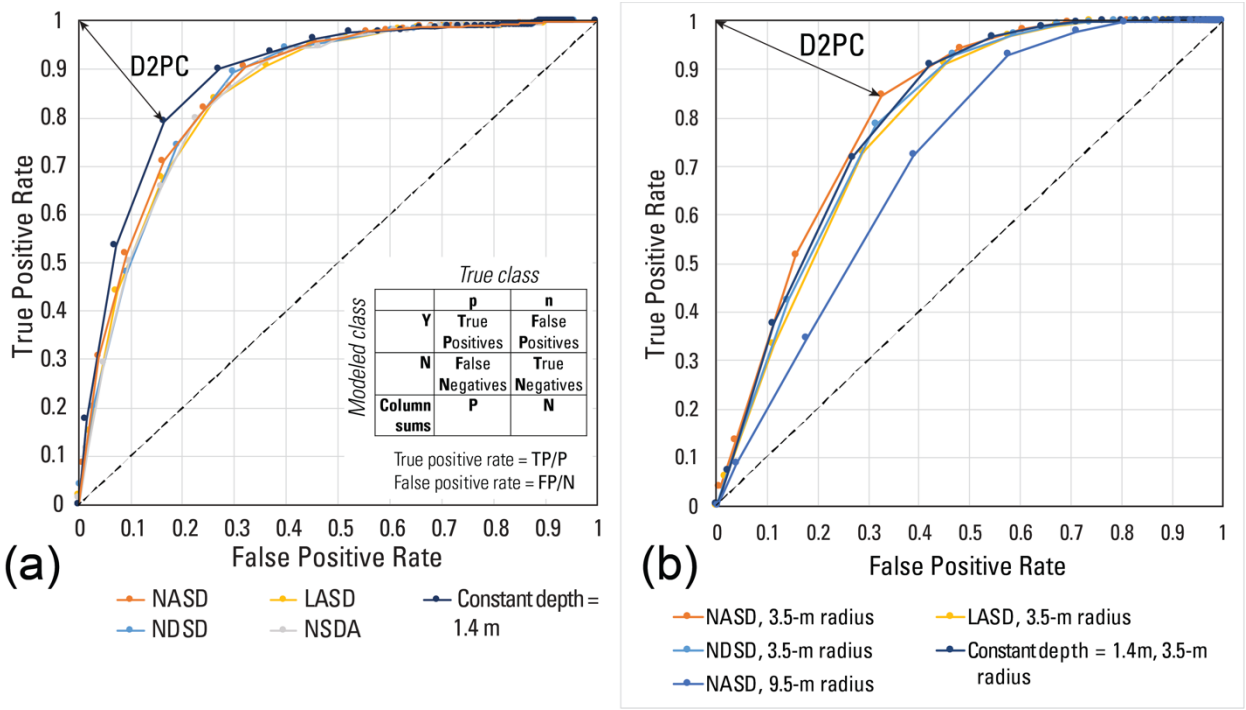

Figure 12. Graphs of true positive rate (TPR) versus false positive rate (FPR) for factor of safety maps in Naranjito calibration area (NAR in Fig. 1a, 1c). Inset shows confusion matrix and formulas defining true positive rate and false positive rate. Double-headed arrow indicates distance to perfect classification (D2PC) for the results of the factor of safety with the smallest D2PC. (a) TPR-FPR results for 1D factor of safety (F_1) in Fig. 10, as well as results for F_1 using other soil-depth models that were tested during the calibration process. (b) TPR-FPR results for quasi-3D factor of safety (F_3) in Fig. 11, as well as results for F_3 using other soil depth models and one with a larger (NASD, 9.5-m radius) trial surface. [Soil-depth models: LASD, linear area- and slope-dependent model (Ho et al. 2012); NASD, modified nonlinear area- and slope-dependent model (modified from Pelletier and Rasmussen 2009); NDSD, nonlinear depth- and slope-dependent model (Pelletier and Rasmussen 2009); NSD, nonlinear slope-dependent model (Pelletier and Rasmussen 2009); NSDA, nonlinear slope-dependent model with linear area dependence (modified by Baum et al. 2021 from NSD model of Pelletier and Rasmussen 2009)].

4.6 Susceptibility categories and predictive strength

Computing F_3 over the combined study areas of Lares, Utuado, and Naranjito municipalities produced somewhat different results than in the calibration areas. Calibration areas have very high landslide densities, with average density of 182 scarps/km^2 at NAR. However, landslide density varies considerably across each municipality. Based on positive correlation between low F_3 and landslide scarp points mapped by Hughes et al. (2019), we established susceptibility categories based on percentages of landslides enclosed by successive susceptibility categories as noted previously and as shown in Table 4. Increasing density of observed landslides is consistent with increasing susceptibility. Very high susceptibility (typically > 118 scarp points/km^2) characterizes 23% of the total study area and 21%, 43%, and 45% of the area underlain by marine volcaniclastic, submarine basalt, and granitoid rocks, respectively. Almost all karst areas underlain by limey sediments had low susceptibility (< 2 scarp points/km^2) (Baxstrom et al. 2021b). Based on the information in Table 4, the AUC for the entire map area is 0.84, and D2PC is 0.34.

Recent, detailed mapping of source areas provided an opportunity to further test performance of the pre-Hurricane María F_3 map (section 3.9, Fig. 4). Figure 13 shows TPR-FPR curves for the pre-Hurricane María F_3 map tested against Hurricane María landslide source polygons (Baxstrom et al. 2021a; Einbund et al. 2021a, 2021b) and against

699 scarp points (Table 4). The AUC range, 0.85 – 0.88, is somewhat greater than obtained by testing within a 3-m radius
700 of the scarp points, 0.84.
701
702 **Table 4. Landslide susceptibility categories based on minimum value of quasi-3D factor of safety, F_3, within a 3-m radius**
703 **of landslide scarp points mapped by Hughes et al. (2019) for all three municipalities. For consistency, F_3 thresholds below**
704 **are based on F_3 calculated using pre-Hurricane María lidar topography and scarp locations of landslides induced by**
705 **Hurricane María.**

Landslide Susceptibility	F_3 threshold	Landslide scarp points enclosed (percent)	Landslide scarp points enclosed within increment (number)	Area within increment (km^2)	Landslide points within increment (percent)	Incremental Landslide density (scarps/km^2)
Very High	≤ 0.87	75	27370	232	75	118
High	≤ 0.97	90	5474	108	15	51
Moderate	≤ 1.05	95	1825	68	5	27
Low	> 1.05	100	1824	610	5	3
Total	$0 < F_3 \leq 10$	100	36493	1018	100	36

706

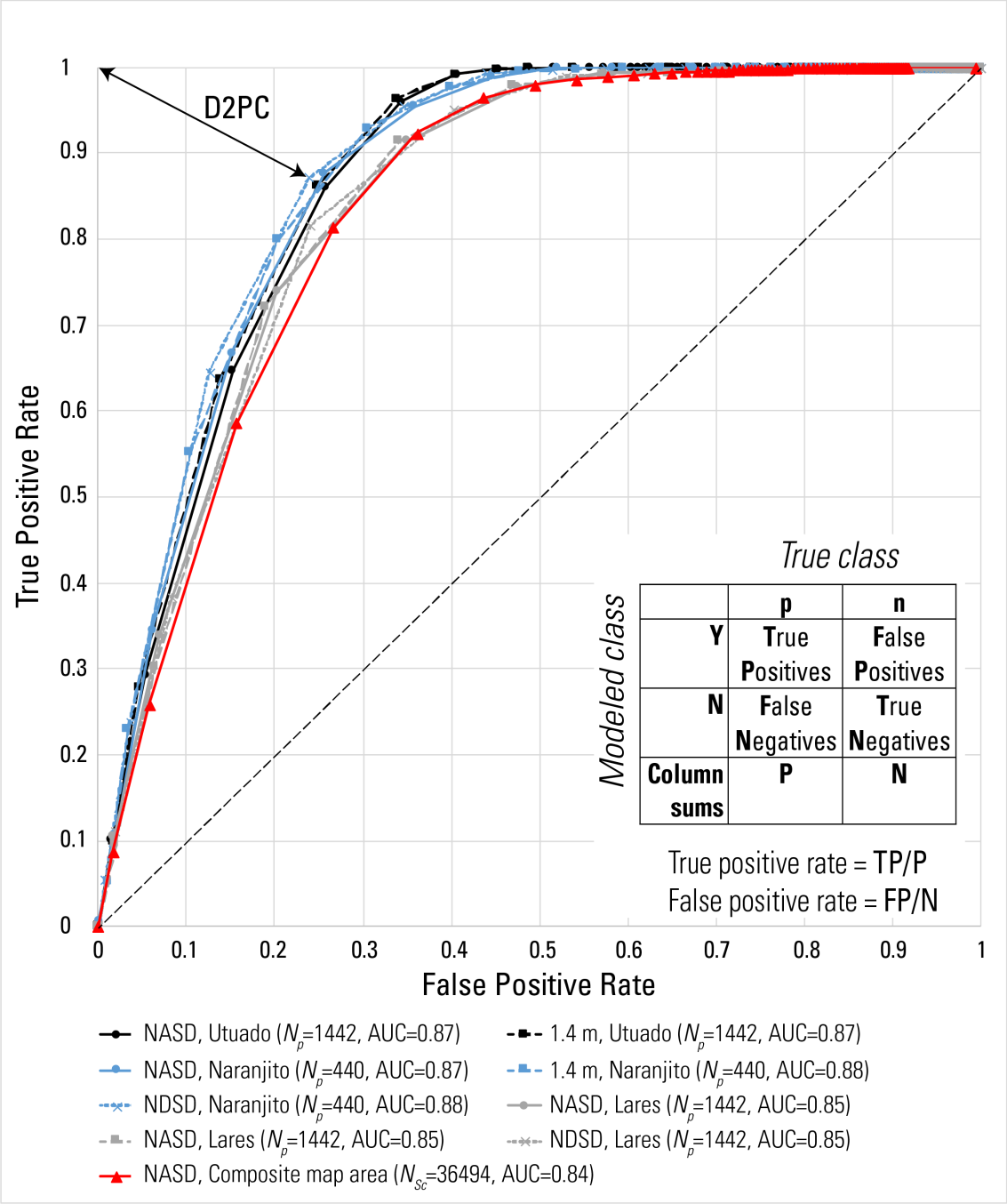

Figure 13. Graph of true positive rate versus false positive rate for pre-Hurricane María susceptibility models across the study area tiles tested against head-scarp points (Hughes et al. 2019) and source polygons for Lares (Einbund et al. 2021b), Naranjito (Baxstrom et al. 2021a), and Utuado (Einbund et al. 2021a) with confusion matrix and formulas defining true positive rate (TPR) and false positive rate (FPR). Double-headed arrow indicates distance to perfect classification (D2PC) for Naranjito source polygons and F_3 computed using NDSD soil depth. True positive rates are based on minimum value of the quasi-3D factor of safety, F_3, within the mapped source polygons or within a 3-m radius of the scarp points. Results for scarp points cover the final pre-Hurricane María susceptibility maps of Lares, Utuado, and Naranjito municipalities. Results for the landslide source polygons cover parts of the component tiles (Fig. 1). Landslide source mapping for Lares and Utuado (Einbund et al. 2021a, b) are near LAR and UTU (LAR2, UTU2, Fig. 1b). The graph compares F_3 performance based on the modified nonlinear area- and slope-dependent (NASD, modified from Pelletier and Rasmussen 2009) soil-depth model and two alternates: constant depth of 1.4 m, and the nonlinear depth- and slope-dependent soil-depth model

(NDSD, Pelletier and Rasmussen 2009), with strength parameters and other inputs held constant. AUC denotes area under the curve of TPR versus FPR, N_p is the number of landslide source polygons, and N_{Sc} is the number of scarp points.

5 Discussion

Our analyses presented in the previous section (Sect. 4.6) indicate that the landslide susceptibility assessment successfully identifies areas where high percentages of Hurricane María landslides occurred. In succeeding paragraphs, we discuss some of the strengths, limitations, and unexpected findings of our approach and results.

Optimum ranges of internal friction angles for all three terranes (Fig. 6) are higher than commonly reported, but consistent with measured values of ϕ' for low normal stress (Likos et al. 2010). Most reported values of ϕ' for soils like those in the study area range from 17° to 41° as noted previously (Sec. 3.2) and are usually based on tests at normal stress greater than 100 kPa. In contrast, samples collected at two field monitoring sites tested at low and moderate normal stresses (Smith et al. 2020) using equipment and procedures described by Likos et al. (2010) had high friction angles for low normal stress. Smith et al. (2020) reported $\phi' = 34.8° – 35.5°$ ($c' = 0 – 4.4$ kPa) for two samples tested at effective normal stress, σ'_n, less than 120 kPa, $\phi' = 45.6°$ for a sample tested at $\sigma'_n \leq 30$ kPa, and $\phi' = 53.9°$ for another sample tested at σ'_n, ≤ 7 kPa. Significantly, shear stress was considerably higher than normal stress for nearly all individual tests at $\sigma'_n \leq 15$ kPa, and many at $\sigma'_n \leq 30$, consistent with $\phi' > 45°$ at low normal stress. In addition to evidence for high internal friction angles at low normal stress, which is particularly relevant to abundant thin (< 0.5 m) landslides in Utuado, three other factors could contribute to stability and reduce the magnitude of ϕ' required to explain stability during dry conditions: (1) Soil suction measured at the sites between rainfall (Smith et al. 2020) indicates that suction stress probably contributes to stability. Preliminary tests indicate that considering modest amounts of suction stress (less than a few tens of kilopascals) during dry conditions in the analysis depicted by Fig. 6 shifts the cells having high TPR toward lower ranges of ϕ'. For example, increasing initial suction stress by -1 kPa shifts the optimum range of ϕ' to 35° – 40° for the submarine basalt and chert landslides compared to the 45° – 50° range in Fig. 6d. (2) Root resistance also likely contributes to slope stability to depths of about 0.5 – 0.6 m. Due to high annual rainfall, vegetation in the study areas tends to be shallow-rooted so that significant root resistance would decline rapidly below about 0.4 – 1.1 m depth (Simon et al. 1990; Larsen 2012). (3) Lateral stress variation also contributes to slope stability. Even in quasi-3D limit-equilibrium as used in computing F_3, combined resistance of neighboring grid cells (columns) and toe wedge contributes to stability and reduces the values of ϕ' and (or) c' needed to achieve stability of a potential landslide under dry conditions (Tables 2 and 3). Quantifying the contributions of these three factors (soil suction, root resistance, and lateral stress) to slope stability could lead to greater refinement of our approach to mapping landslide susceptibility.

Our modelling workflow makes a few trade-offs to create a relatively conservative map of potential landslide sources that accounts for uncertainties. These trade-offs are between speed and simplicity of the assessment, statistical accuracy, and continuity of susceptibility zones. Some of the modelling steps (soil depth and F_3) add complexity, increase time needed to model susceptibility, and slightly reduce performance metrics (AUC and D2PC) compared to F_1 with constant soil depth. In exchange, soil depth and F_3 create more continuous susceptibility zones, join neighboring groups of high-susceptibility pixels, and eliminate isolated, commonly errant, pixels of high landslide

755 susceptibility (Fig. 10 and 11). The increased continuity of the susceptibility zones makes them easier to implement
756 in land use and emergency management. In addition, the potential source areas delineated on the map by the high and
757 very high susceptibility areas provide areas susceptible to shallow landslides for estimating potential landslide runout
758 and debris-flow inundation (Brien et al. 2021). Much of the reduction in AUC for F_3 results from using the minimum
759 factor of safety value computed for any trial landslide that includes a grid cell. Consequently, very high and high
760 susceptibility zones for F_3 are broader than for F_1 and thereby have a buffer along their edges. Nevertheless, as
761 indicated by various performance metrics and landslide densities in the susceptibility classes, the landslide assessment
762 successfully distinguishes areas having different levels of susceptibility to landslide initiation (Tables 3, 4) despite
763 these trade-offs.
764 Although F_1 for constant depth has slightly better performance metrics (the highest AUC and smallest D2PC) than F_1
765 for any of the soil depth models calibrated to landslide source depths (Table 2, Fig. 12a) at NAR, its performance
766 metrics are comparable to the nonlinear soil-depth models elsewhere. Our field observations indicate that depth of
767 shallow, rainfall-induced landslides is well correlated to depth of mobile regolith ("soil") due to strength and
768 permeability contrasts at its base. Soil-depth models represent the distribution of soil depth more consistently with
769 field conditions than constant depth in many settings (Pelletier and Rasmussen 2009; Ho et al. 2012; Catani et al.
770 2010; Nicótina et al. 2011; Gomes et al. 2016; Patton et al. 2018). Performance metrics (ED = $\sqrt{2}$; mean-squared error,
771 MSE = σ_o^2) indicate average depth was a poorer predictor of observed landslide depth than any of the models Tello
772 (2020) tested for Utuado. Despite odd differences in how the models estimate soil depth on mid-slope benches and
773 flat valley bottoms, the models we tested (NASD, NSDA, NDSD, LASD) predict thinner soils on ridge crests and
774 thicker soils in hillside hollows, consistent with patterns observed in Puerto Rico and elsewhere for dissected
775 topography (Roering 2008). For example, mean depths of landslide sources from field mapping in Puerto Rico were
776 3.25 m (for concave slopes), 2.5 m (for convex slopes), 2.7 m (for planar slopes; Schulz et al. 2023). The unexpected,
777 good performance of F_1 for constant soil depth at NAR points out limitations of soil depth models and may result in
778 part from widespread modifications to the landscape resulting from agriculture, road (e.g., Ramos-Scharrón et al.
779 2021) and building construction, and other activities. Effects of these activities may have influenced the locations of
780 shallow landslides sufficiently to weaken correlation between landslide location and topographic features that
781 influence soil depth (as at LAR and ANA, Fig. 8a). The high degree of slope modification (roads and terraces) in the
782 NAR calibration area is likely a determining factor in F_1 performance there (Fig. 10). Identifying specific areas or
783 features where constant-depth F_1 classifies susceptibility differently than F_1 with other soil-depth models might reveal
784 potential improvements.
785 Computing F_1 using the modified NASD soil-depth model resulted in the areas assigned to the moderate, high, and
786 very high susceptibility classes being more clearly delineated with little or no loss of performance compared to using
787 constant depth. The susceptibility zones in the constant-depth F_1 susceptibility map (Fig. 10b) are more diffuse or
788 fragmented (less continuous) than for the NASD soil depth (Fig. 10a) and other soil models we tested. Fragmentation
789 also occurred for susceptibility zones defined by slope categories (Fig. S3a). As noted previously, this improved
790 delineation came with only a slight reduction in AUC (0.88 to 0.86) and small increase in D2PC (0.26 to 0.30) for
791 NAR. When applied to the entire DEM tile covering Naranjito municipality, performance of F_1 for constant depth and

792 F_1 for NASD tied with each other and with slope categories (AUC = 0.87, D2PC = 0.29 - 0.30). As noted previously,
793 when checked against detailed source mapping, the performance metrics for F_3 are better than when compared against
794 the scarp points (Fig. 13). In addition, differences in performance metrics between constant depth and the NDSD
795 model and modified NASD model are negligible.
796 Due to physical (subsurface conditions, ground-failure mechanisms) and conceptual (parameters, models)
797 uncertainties, the F_3 value at the boundary between high and moderate susceptibility is slightly less than 1 (0.97, Table
798 4). Although the strength parameters could be increased to achieve $F_3 = 1.0$ at TPR = 0.90, we also wanted to keep F3
799 at TPR = 0.95 relatively low while keeping $F_3 > 1$ under dry conditions for as much area as possible. Our final model
800 parameters represent a compromise between stable slopes ($F_3 > 1$) under dry conditions and low factor of safety (F_3
801 < 1) for highly susceptible slopes under presumed wettest conditions.
802 Other things being equal, the quasi-3D stability analysis, F_3, has a somewhat smaller AUC and larger D2PC, compared
803 to F_1 (Tables 2 and 3), but improves the final map. The improvements are better separation between the different
804 susceptibility classes (Fig. 10 and 11) and a slightly more conservative map compared to F_1, which is helpful for life-
805 safety based land use planning and emergency response scenarios. With AUC=0.80 and D2PC=0.38 for F_3 based on
806 the modified NASD soil-depth and 3.5 m radius for the trial surface (Table 3), F_3 successfully identifies potential
807 landslide sources at NAR. For the entire map area, the AUC (0.84) and D2PC (0.33) scores are slightly better (Table
808 4, Fig. 13), due in part to the large area of low landslide susceptibility that is underlain by limey sediments and
809 characterized by cone karst. By considering slope stability at the scale of representative landslide sources (median
810 area, Fig. 3c), F_3 eliminates isolated grid cells and tiny clusters of 2 – 4 cells that likely are classified incorrectly by
811 F_1 as highly or very highly susceptible due to locally steep slopes at the pixel scale (1 m). Such isolated cells and
812 clusters could be eliminated after analysis, but boundaries of susceptible areas would remain somewhat ragged. In
813 contrast our approach provides an objective method for eliminating the isolated pixels and smoothing the boundaries.
814 F_3 bridges gaps between neighboring areas of low F_1 and thereby maps susceptible areas that are more continuous and
815 with smoother, more definite boundaries than F_1. Thus, F_3 further improves delineation of susceptible areas beyond
816 improvements achieved by using the modified NASD soil-depth model with F_1. Maps having continuous, clearly
817 delineated areas assigned to each susceptibility class such as those obtained by using F_3 reduce guesswork in making
818 land use and emergency management decisions by eliminating the ragged, transitional boundaries obtained with F_1.
819 For example, to compare the insets in Figs. 10 and 11 to each other as well as slope categories (Fig. S3a) and F_3 based
820 on the NDSD soil-depth model (Fig. S3d), see Fig. S3b, c, e and f. Alternately continuous, clear delineation can be
821 achieved by aggregating raster maps to slope units (Alvioli et al. 2016; Woodard et al. 2024).Nevertheless, an added
822 benefit of using F_3 is creation of well-defined potential landslide source areas that allow estimation of areas susceptible
823 to potential downslope runout and downstream inundation (Brien et al. 2021). Performance metrics for F_3 considering
824 detailed source mapping (Fig. 13) are sufficiently high ($0.85 \leq AUC \leq 0.88$) to consider F_3 a very successful indicator
825 of landslide susceptibility in our study area. As the basis for our final susceptibility maps, we selected the F_3 map
826 derived from the modified NASD soil depth model (Fig. 11a) because of its high AUC combined with its well-defined
827 source areas and the realistic modeled soil depths for estimating potential landslide volumes. Visual comparison

828 indicates only slight differences between F_3 maps based on pre-event and post-event DEMs (Fig. S4). Model input
829 parameters for the final maps are summarized in Supplemental Figures S1 and S2.
830 The susceptibility analysis portrayed in Fig. 11 and our final maps (Supplemental Figures S1 and S2) are valid
831 throughout the three municipalities despite the variable density of Hurricane María landslides throughout the map area
832 (Bessette-Kirton et al. 2017; Hughes et al. 2019) and within each susceptibility class. High landslide density generally
833 corresponds to low F_3 (Table 4); however, not all susceptible areas were equally affected by Hurricane María. Thus,
834 although some areas of low F_3, particularly in Naranjito, had low landslide density, the low density does not invalidate
835 the susceptibility assessment of the potential for future landslides. Factors such as antecedent soil moisture are known
836 to have affected the density of landslides induced by Hurricane María (Bessette-Kirton et al. 2019a) and were
837 addressed in the statistically based island-wide landslide susceptibility assessment of Hughes and Schulz (2020a).
838 Notably Naranjito had much lower root-zone soil moisture immediately after the hurricane than Utuado and Lares
839 (Fig. 26 of Hughes and Schulz 2020a). Variable rainfall intensity and duration are also known to affect landslide
840 response of susceptible areas (Larsen and Simon 1993; Pando et al. 2005). Intensity and duration are known to have
841 varied during Hurricane María, causing further differences in landslide density. Our assessment considered fully
842 saturated conditions with the water table at the ground surface to depict likely wettest-case soil moisture effects,
843 including high antecedent soil wetness, as well as high intensity and long-duration rainfall. Thus, it was not necessary
844 to specifically model antecedent soil moisture conditions. Less-severe conditions may produce landslides in the same
845 general areas as predicted by our assessment, however, in lower numbers than observed following Hurricane María.
846 Setting the boundaries between susceptibility classes based on F_1 or F_3 corresponding to specific values of TPR rather
847 than setting boundaries based on theoretical values of F_1 or F_3 (such as $F_3 = 1.0$) reduces uncertainty and ensures
848 correspondence between landslide density and degree of landslide susceptibility. Soil, saprolite, and bedrock are
849 inherently heterogenous. Their hydraulic and strength properties (and corresponding parameters) vary spatially at all
850 scales (Terzaghi et al. 1996). Other studies have applied probabilistic approaches and sensitivity analyses have been
851 applied successfully to address parameter uncertainty and improve accuracy of physically based modelling of landslide
852 susceptibility (Raia et al. 2014; Zieher et al. 2017; Canli et al. 2018). Many parameter combinations (c' and ϕ') can
853 achieve similar levels of predictive accuracy in computing F_1 for observed distributions of landslide slope and depth
854 (Baum et al. 2019; Baum 2021). These and other uncertainties such as transient pore-water pressures, subsurface
855 features, heterogeneity, and other factors, weaken the link between theoretical values of F_1 or F_3 and estimated
856 likelihood of failure for site-specific cases when applying limit-equilibrium slope stability analysis over wide areas.
857 On the other hand, maps classified based on TPR have a strong link to susceptibility. Such maps are readily comparable
858 to each other when F_1 or F_3 values are computed with different parameters, as they show like outcomes (areas that
859 capture 75%, 90% and 95% of observed landslides in this study). Comparing like outcomes focuses on differences
860 and uncertainties that affect the quality of the susceptibility assessment that might be masked by comparing the maps
861 when classified using the same F_1 or F_3 values. In this study, low values of F_1 and F_3 correspond to high observed
862 Hurricane María landslide density (Table 4), as would be expected. The selected boundaries for susceptibility classes
863 ensure a meaningful distinction between average landslide density in the successive classes (Table 4).

The susceptibility map correctly predicts locations of most landslides that are deeper than 3 m, despite the maximum modeled soil depth of 3 m more typical of shallow landslides. Ten of the landslides summarized in Fig. 3e are deeper than 3 m. Most (nine) are within the Naranjito tile (Fig. 1), and the other is in Lares. The mapped point on each landslide headscarp and adjoining or surrounding slope was within the high or very high susceptibility zone for seven of the ten deep landslides. The other three had head scarps on a gently sloping area (road or pad) that was set back a few meters from the steep slope, but the adjoining slope with the landslide body was within the high and very high susceptibility zones. Although the predicted locations might be right for the wrong reason (predicting a shallow translational landslide rather than a deeper, translational, or rotational landslide), it is nevertheless encouraging that the locations of even the deep landslides are identified for the sake of hazard assessment and planning. This probably occurred because the deep landslides occurred well within the same slope range as other mapped landslides (Fig. 3, 4).

Despite the simplicity of soil and water parameters, the maps successfully predicted the effects from Hurricane María. Calibrating with field data from the small calibration areas (ANA, LAR, UTU, and NAR, Fig. 1) and then testing with the island-wide scarp points (Hughes et al. 2019) confirmed the successes of our approach (Supplemental Figures S1 and S2). Testing with detailed landslide source maps (Baxstrom et al. 2021a; Einbund et al. 2021a, 2021b) strengthens our results even though they cover only a fraction of the study area.

The workflow outlined in Fig. 4 can be simplified in areas where few data are available. An accurate digital elevation model and accurate landslide inventory with measurements of source area size, depth, and slope (Fig. 3) are the most critical data for a landslide susceptibility analysis. Strength parameter ranges can be estimated from landslide source depth and slope (Fig. 5, 6). Soil model calibration can be bypassed by assuming constant average landslide source depth. Strength parameters can then be refined using the procedure described in Sect. 3.5. Alternately a soil model and strength parameters can be calibrated simultaneously to the inventory as we did for the NAR calibration area. Calculation of pressure head, F_1 and F_3 can then proceed as outlined in Sect. 3.4.2, 3.4.3, 3.4.4, and 3.9, followed by validation and evaluation (Sect. 3.11). Compared to a map based on the simplest of landslide susceptibility approach, slope ranges with its ragged, fragmented susceptibility zones, our procedure creates cohesive landslide susceptibility zones that have smooth, buffered boundaries with only a slightly lower AUC score (0.84) than for slope (0.87) across the entire study area.

6 Conclusions

We defined a workflow for assessing landslide susceptibility using multiple modelling stages and successfully applied it using high-resolution (1-m) topography over a large (about 1000 km^2) geographic area in the central mountains of Puerto Rico (Fig. 1). The workflow includes modelling soil depth, pressure head, and limit-equilibrium slope stability (Fig. 4). Although calibration studies showed that assuming constant average soil depth as input for 1D (infinite-slope) factor of safety against landsliding, F_1, gave the best performance metrics in a 2.5 km^2 calibration area, use of a soil-depth model more clearly delineated areas susceptible to landslide initiation with only a modest reduction in the AUC from 0.88 to 0.86. Using a quasi-3D limit-equilibrium slope stability analysis, the factor of safety, F_3, further refined the susceptibility assessment by more clearly delineating boundaries between the different susceptibility classes and

by assessing stability at the scale of the observed median-sized landslides. Despite further reduction in AUC to 0.80 for the NAR calibration area, the map based on F_3 is more readily usable in certain applications than a map based on F_1, and it still performs well as a classifier of landslide susceptibility. Performance metrics for the F_3 map of the entire ~1000 km^2 study area, AUC = 0.84 and D2PC = 0.34, are slightly better than results at the NAR calibration area. Performance measured against detailed source mapping of selected areas is even better: 0.85 ≤ AUC ≤ 0.88 and 0.27 ≤ D2PC ≤ 0.33. These metrics indicate the map is suitable for planning, regulation, and emergency preparedness decisions at the municipality scale. The map may also be used to assess hazards, such as ground collapse, resulting from landslide initiation. Source area delineation as shown on maps may also be used for defining landslide starting locations and surface area needed to assess areas with potential downslope movement of sediment mobilized by future landslides.

Code availability

Computer codes used in this study are available from the U.S. Geological Survey software repository as follows: TRIGRS 2.1, https://doi.org/10.5066/F7M044QS; REGOLITH, https://doi.org/10.5066/P9U2RDWJ; and Slabs3D, https://doi.org/10.5066/P9G4I8IU.

Data availability

The pre-event (2015) and post-event (2018) lidar topographic data used in this study are available through the National Map at https://apps.nationalmap.gov/lidar-explorer/#/. Soil mapping databases used to estimate soil properties are available from the Natural Resources Conservation Service at https://www.nrcs.usda.gov/resources/data-and-reports/web-soil-survey. Other data are available from the U.S. Geological Survey ScienceBase digital repository as follows: Summaries of geotechnical data, https://doi.org/10.5066/P9UXTQ4B; model input and output raster grids and model parameter input files used to produce the large maps (Supplemental Figures S1 and S2), https://doi.org/10.5066/P9C1U0LP; Landslide head scarp points, https://doi.org/10.5066/P9BVMD74; landslide polygons, https://doi.org/10.5066/F7JD4VRF, https://doi.org/10.5066/P9GBGA4I, https://doi.org/10.5066/P9YYU7W1, https://doi.org/10.5066/P9EASZZ7, and https://doi.org/10.5066/P9ZNUR1P.

Author contribution

RB, WS, MR and DB planned the study. WS managed the project. MT carried out model calibrations. RB developed the model code, carried out the simulations, and computed the model performance statistics. DB, WS, MR, MT, and RB analyzed the data. RB wrote the manuscript draft; DB, MR, and WS reviewed and edited the manuscript.

Competing interests

The authors declare that they have no conflict of interest.

Disclaimer

Any use of trade, firm, or product names is for descriptive purposes only and does not imply endorsement by the U.S. Government.

Acknowledgements

Adrian Lewis compiled and summarized geotechnical data from published and publicly available sources. Mason Einbund extracted statistics on landslide true positives and density from pre-Hurricane María factor of safety grids. Emily Bedinger generated flow-accumulation raster grids and edited the model output grids to remove edge effects. Brian Collins and Lauren Schaefer reviewed an earlier version of this manuscript. This work was supported in part by the Additional Supplemental Appropriations for Disaster Relief Requirements Act, 2018 (P.L. 115-123)

References

Aaron, J., McDougall, S., Moore, J.R., Coe, J.A., and Hungr, O.: The role of initial coherence and path materials in the dynamics of three rock avalanche case histories, Geoenvironmental Disasters, 4, 5. https://doi.org/10.1186/s40677-017-0070-4, 2017.

Alvioli, M., and Baum, R.L.: Parallelization of the TRIGRS model for rainfall-induced landslides using the message passing interface. Environ. Modell. Softw. 81, 122–135. https://doi.org/10.1016/j.envsoft.2016.04.002, 2016.

Alvioli, M., Marchesini, I., Reichenbach, P., Rossi, M., Ardizzone, F., Fiorucci, F., and Guzzetti, F.: Automatic delineation of geomorphological slope units with r.slopeunits v1.0 and their optimization for landslide susceptibility modeling, Geosci. Model Dev., 9, 3975–3991, https://doi.org/10.5194/gmd-9-3975-2016, 2016.

Arnone, E., Noto, L., Lepore, C., Bras, R.: Physically-based and distributed approach to analyze rainfall-triggered landslides at watershed scale, Geomorphology, 133, 121–131, https://doi.org/10.1016/j.geomorph.2011.03.019, 2011.

ASTM International: D2487-17e1, Standard Practice for Classification of Soils for Engineering Purposes (Unified Soil Classification System), https://doi.org/10.1520/D2487-17E01, 2020.

Baum, R.L.: Rapid sensitivity analysis for reducing uncertainty in landslide hazard assessments, in: Understanding and Reducing Landslide Disaster Risk, edited by: Guzzetti, F., Mihalić Arbanas, S., Reichenbach, P., Sassa, K., Bobrowsky, P.T., and Takara, K., Springer, Cham, Switzerland, 329–335, https://doi.org/10.1007/978-3-030-60227-7_37, 2021.

Baum, R.L.: Slabs3D—A Fortran 95 program for analyzing potential shallow landslides in a digital landscape, U.S. Geol. Surv. software release [code], https://doi.org/10.5066/P9G4I8IU, 2023.

Baum, R.L., and Lewis, A.C.: Engineering soil classification and geotechnical measurements in Lares, Naranjito, and Utuado, Puerto Rico: U.S. Geol. Surv. data release [data set], https://doi.org/10.5066/P9UXTQ4B, 2023.

Baum, R.L., Brien, D.L., Reid, M.E., Schulz, W.H., Tello, M.J., and Bedinger, E.C.: Model input and output data covering Lares Municipio, Utuado Municipio, and Naranjito Municipio, Puerto Rico, for landslide initiation susceptibility assessment after Hurricane Maria: U.S. Geol. Surv. data release [data set], https://doi.org/10.5066/P9C1U0LP, 2023.

964 Baum, R.L., Savage, W.Z., and Godt, J.W.: TRIGRS—A Fortran program for transient rainfall infiltration and grid-
965 based regional slope-stability analysis, version 2.0, U.S. Geol. Surv. Open-File Report 2008-1159, 75 pp.
966 https://doi.org/10.3133/ofr20081159, 2008.
967 Baum, R.L., Godt, J.W., and Savage, W.Z.: Estimating the timing and location of shallow rainfall-induced landslides
968 using a model for transient, unsaturated infiltration. Journal of Geophysical Research: Earth Surface, 115(F3), F03013.
969 https://doi.org/10.1029/2009JF001321, 2010.
970 Baum, R.L., Godt, J.W., Coe, J.A., and Reid, M.E.: Assessment of shallow landslide potential using 1D and 3D slope
971 stability analysis, in: Landslides and Engineered Slopes: Protecting Society through Improved Understanding, edited
972 by: Eberhardt, E., Froese, C., Turner, A.K., and Leroueil, S., Taylor & Francis Group, London, pp. 1667–1672, ISBN
973 978-0-415-62123-6, 2012.
974 Baum, R.L., Schulz, W.H., Brien, D.L., Burns, W.L., Reid, M.E., and Godt, J.W.: Progress in regional landslide hazard
975 assessment—Examples from the USA, in: Landslide Science for a Safer Geoenvironment , edited by, Sassa, K.,
976 Canuti, P., and Yin, Y., Springer, Cham, Switzerland, pp. 21–36. https://doi.org/10.1007/978-3-319-04999-1_2, 2014.
977 Baum, R.L., Cerovski-Darriau, C., Schulz, W.H., Bessette-Kirton, E., Coe, J.A., Smith, J.B., and Smoczyk, G.M.:
978 Variability of hurricane María debris-flow source areas in Puerto Rico—Implications for hazard assessment, AGU
979 Fall Meeting, Washington, DC 2018, NH14A-02, https://agu.confex.com/agu/fm18/meetingapp.cgi/Paper/412740,
980 2018.
981 Baum, R.L., Scheevel, C.R., and Jones, E.S.: Constraining parameter uncertainty in modeling debris-flow initiation
982 during the September 2013 Colorado Front Range storm, in: Debris-flow Hazards Mitigation: Mechanics, Monitoring,
983 Modeling, and Assessment, edited by: Kean, J.W., Coe, J.A., Santi, P.M., and Guillen, B.K., Association of
984 Environmental and Engineering , Brunswick, Ohio, pp. 249–256, https://doi.org/10.25676/11124/173212, 2019.
985 Baum, R.L., Bedinger, E.C., and Tello, M.J.: REGOLITH--A Fortran 95 program for estimating soil mantle thickness
986 in a digital landscape for landslide and debris-flow hazard assessment, U.S. Geol. Surv. software release [code],
987 https://doi.org/10.5066/P9U2RDWJ, 2021.
988 Bawiec, W.J.: Geologic terranes of Puerto Rico, in: Geology, geochemistry, geophysics, mineral occurrences, and
989 mineral resource assessment for the commonwealth of Puerto Rico, edited by: Bawiec W.J., U.S. Geol. Surv. Open-
990 File Rep. 98–38. https://doi.org/10.3133/ofr9838, 1998.
991 Baxstrom, K.W., Einbund, M.M., and Schulz, W.H.: Map data from landslides triggered by Hurricane María in a
992 section of Naranjito, Puerto Rico, U.S. Geol. Surv. data release [data set], https://doi.org/10.5066/P9GBGA4I, 2021a.
993 Baxstrom, K.W., Einbund, M.M., and Schulz, W.H.: Map data from landslides triggered by Hurricane María in the
994 greater karst region of northwest Puerto Rico, U.S. Geol. Surv. data release [data set],
995 https://doi.org/10.5066/P9YYU7W1, 2021b.
996 Begueria, S.: Validation and evaluation of predictive models in hazard assessment and risk management. Nat. Hazards,
997 37, 315–329. https://doi.org/10.1007/s11069-005-5182-6, 2006.
998 Benda, L., Miller, D., Andras, K., Bigelow, P., Reeves, G., and Michael, D.: NetMap: A new tool in support of
999 watershed science and resource management, Forest Sci., 53(2), 206-219.
1000 https://doi.org/10.1093/forestscience/53.2.206, 2007.

1001 Bessette-Kirton, E.K., Coe, J.A., Godt, J.W., Kean, J.W., Rengers, F.K., Schulz, W.H., Baum, R.L., Jones, E.S., and
1002 Staley, D.M.: Map data showing concentration of landslides caused by hurricane María in Puerto Rico. U.S. Geol.
1003 Surv. data release [data set], https://doi.org/10.5066/F7JD4VRF, 2017.
1004 Bessette-Kirton, E.K., Cerovski-Darriau, C., Schulz, W.H., Coe, J.A., Kean, J.W., Godt, J.W., Thomas, M.A., and
1005 Hughes, K.S.: Landslides triggered by Hurricane María: Assessment of an extreme event in Puerto Rico, GSA Today,
1006 29, 4–10. https://doi.org/10.1130/GSATG383A.1, 2019a.
1007 Bessette-Kirton, E.K., Kean, J.W., Coe, J.A., Rengers, F.K., and Staley, D.M.: An evaluation of debris-flow runout
1008 model accuracy and complexity in Montecito, California: Towards a framework for regional inundation-hazard
1009 forecasting, in: Debris-flow Hazards Mitigation: Mechanics, Monitoring, Modeling, and Assessment, edited by: Kean,
1010 J.W., Coe, J.A., Santi, P.M., Guillen, B.K., Association of Environmental and Engineering Geologists, Brunswick,
1011 Ohio, pp. 257–264. https://doi.org/10.25676/11124/173211, 2019b.
1012 Bessette-Kirton, E.K., Coe, J.A., Kelly, M.A., Cerovski-Darriau, C., and Schulz, W.H.: Map data from landslides
1013 triggered by Hurricane María in four study areas of Puerto Rico. U.S. Geol. Surv. data release [data set].
1014 https://doi.org/10.5066/P9OW4SLX, 2019c.
1015 Bessette-Kirton, E.K., Coe, J.A., Schulz, W.H., Cerovski-Darriau, C., and Einbund, M.M.: Mobility characteristics of
1016 debris slides and flows triggered by Hurricane María in Puerto Rico, Landslides 17, 2795–2809,
1017 https://doi.org/10.1007/s10346-020-01445-z, 2020.
1018 Brien, D.L., Reid, M.E., Cronkite-Ratcliff, C., and Perkins, J.P.: Portraying runout and inundation from hurricane-
1019 induced landslides in Puerto Rico, Geological Society of America Abstracts with Programs. 53(6), 85-4,
1020 https://doi.org/10.1130/abs/2021AM-368632, 2021.
1021 Catani, F., Segoni, S., and Falorni, G.: An empirical geomorphology-based approach to the spatial prediction of soil
1022 thickness at catchment scale, Water Resour. Res., 46(5), W05508, https://doi.org/10.1029/2008WR007450, 2010.
1023 Canli, E., Mergili, M., Thiebes, B., and Glade, T.: Probabilistic landslide ensemble prediction systems: Lessons to be
1024 learned from hydrology, Nat. Hazard. Earth Sys., 18(8), 2183–2202, https://doi.org/10.5194/nhess-18-2183-2018,
1025 2018.
1026 Carrara, A., Guzzetti, F., Cardinali, M., and Reichenbach, P.: Use of GIS technology in the prediction and monitoring
1027 of landslide hazard, Nat. Hazards, 20, 117–135, https://doi.org/10.1023/A:1008097111310, 1999.
1028 Chung, C.F., and Fabbri, A.G.: Validation of spatial prediction models for landslide hazard mapping, Nat. Hazards,
1029 30, 451–472, https://doi.org/10.1023/B:NHAZ.0000007172.62651.2b, 2003.
1030 DeRose, R.C., Trustrum, N.A., and Blaschke, P.M.: Geomorphic change implied by regolith-slope relationships on
1031 steepland hillslopes, Taranaki, New Zealand, Catena, 18, 489-514, https://doi.org/10.1016/0341-8162(91)90051-X,
1032 1991.
1033 Einbund, M.M., Baxstrom, K.S., and Schulz, W.H.: Map data from landslides triggered by Hurricane María in four
1034 study areas in the Utuado municipality, Puerto Rico, U.S. Geol. Surv. data release [data set],
1035 https://doi.org/10.5066/P9ZNUR1P, 2021a.

1036 Einbund, M.M., Baxstrom, K.S., and Schulz, W.H.: Map data from landslides triggered by Hurricane María in four
1037 study areas in the Lares municipality, Puerto Rico. U.S. Geol. Surv. data release [data set],
1038 https://doi.org/10.5066/P9EASZZ7, 2021b.
1039 Ellen, S.D., Mark, R.K., Cannon, S.H., and Knifong, D.L.: Map of debris-flow hazard in the Honolulu District of
1040 Oahu, Hawaii, U.S. Geol. Surv. Open-File Rep. 93-213, 28 pp., https://doi.org/10.3133/ofr93213, 1993.
1041 Fan, L., Lehmann, P., McArdell, B., and Or, D.: Linking rainfall-induced landslides with debris flows runout patterns
1042 towards catchment scale hazard assessment, Geomorphology 280, 1-15.
1043 https://doi.org/10.1016/j.geomorph.2016.10.007, 2017.
1044 Fawcett, T.: An introduction to ROC analysis, Pattern Recogn. Lett., 27(8), 861–874,
1045 https://doi.org/10.1016/j.patrec.2005.10.010, 2006.
1046 Formetta, G., Capparelli, G., and Versace, P.: Evaluating performance of simplified physically based models for
1047 shallow landslide susceptibility, Hydrol. Earth Syst. Sci., 20, 4585–4603, https://doi.org/10.5194/hess-20-4585-2016,
1048 2016.
1049 George, D.L., and Iverson, R.M.: A depth-averaged debris-flow model that includes the effects of evolving dilatancy:
1050 2. Numerical predictions and experimental tests, P. Roy. Soc. A-Math. Phy., 470(2170), 20130820,
1051 https://doi.org/10.1098/rspa.2013.0820, 2014.
1052 Godt, J.W., Schulz, W.H., Baum, R.L., and Savage, W.Z.: Modeling rainfall conditions for shallow landsliding in
1053 Seattle, Washington, in: Landslides and Engineering Geology of the Seattle, Washington, Area, edited by: Baum,
1054 R.L., Godt, J.W., Highland, L.M., Geological Society of America, Boulder, Colorado, 137–152,
1055 https://doi.org/10.1130/2008.4020(08), 2008a.
1056 Godt, J.W., Baum, R.L., Savage, W.Z., Salciarini, D., Schulz, W.H., and Harp, E. L.: Transient deterministic shallow
1057 landslide modeling: Requirements for susceptibility and hazard assessments in a GIS framework, Eng. Geol., 102,
1058 214–226, https://doi.org/10.1016/j.enggeo.2008.03.019, 2008b.
1059 Gomes, G.J.C., Vrugt, J.A., and Vargas, Jr., E.A.: Toward improved prediction of the bedrock depth underneath
1060 hillslopes: Bayesian inference of the bottom-up control hypothesis using high-resolution topographic data, Water
1061 Resour. Res., 52(4), 3085–3112, https://doi.org/10.1002/2015WR018147, 2016.
1062 Gupta, H.V., Kling, H., Yilmaz, K.K., and Martinez, G.F.: Decomposition of the mean squared error and NSE
1063 performance criteria: Implications for improving hydrological modeling. J. Hydrol., 377(1-2), 80–91.
1064 https://doi.org/10.1016/j.jhydrol.2009.08.003, 2009.
1065 Heidemann, H.K.: Lidar base specification (ver. 1.3, February 2018), U.S. Geological Survey Techniques and
1066 Methods, 11, B4, 101 p., https://doi.org/10.3133/tm11b4, 2018.
1067 Ho, J.-Y., Lee, K.T., Chang, T.-C., Wang, Z.-Y., and Liao, Y.-H.: Influences of spatial distribution of soil thickness
1068 on shallow landslide prediction. Eng. Geol., 124, 38–46. https://doi.org/10.1016/j.enggeo.2011.09.013, 2012.
1069 Hovland, H.J.: Three-dimensional slope stability analysis method. J. Geotech. Eng.-ASCE, 103(GT9), 971–986.
1070 https://doi.org/10.1061/AJGEB6.0000493, 1977.
1071 Hsu, Y.C., and Liu, K.F.: Combining TRIGRS and DEBRIS-2D models for the simulation of a rainfall infiltration
1072 induced shallow landslide and subsequent debris flow, Water, 11(5), 890, https://doi.org/10.3390/w11050890, 2019.

Hughes, K.S., Bayouth-García, D., Martínez-Milian, G.O., Schulz, W.H., and Baum, R.L.: Map of slope-failure locations in Puerto Rico after Hurricane María. U.S. Geol. Surv. data release [data set], https://doi.org/10.5066/P9BVMD74, 2019.

Hughes, K.S., and Schulz, W.H.: Map depicting susceptibility to landslides triggered by intense rainfall, Puerto Rico, U.S. Geol. Surv. Open-File Rep. 2020–1022, 91 pp., 1 plate, scale 1:150,000. https://doi.org/10.3133/ofr20201022, 2020a.

Hughes, K.S., Schulz, W.H.: Results from frequency-ratio analyses of soil classification and land use related to landslide locations in Puerto Rico following Hurricane María. U.S. Geol. Surv. data release [data set], https://doi.org/10.5066/P9VK2FAL, 2020b.

Hungr, O., Salgado, F.M., and Byrne, P.M.: Evaluation of a three-dimensional method of slope-stability analysis, Can. Geotech. J., 26(4), 679–686, https://doi.org/10.1139/t89-079, 1989.

Iverson, R.M.: Landslide triggering by rain infiltration, Water Resour. Res., 36(7), 1897–1910, https://doi.org/10.1029/2000WR900090, 2000.

Jibson, R.W.: Debris flows in southern Puerto Rico, in: Landslide processes of the eastern United States and Puerto Rico, edited by: Schultz A.P., and Jibson R.W., Geol. S. Am. S., 236, 29–55, https://doi.org/10.1130/SPE236-p29, 1989.

Jolly, W.T., Lidiak, E.G., Dickin, A.P., and Wu, T.-W.: Geochemical diversity of Mesozoic island arc tectonic blocks in eastern Puerto Rico, in: Tectonics and Geochemistry of the Northeastern Caribbean, edited by: Likiak, E.G., Larue, D.K., Geol. S. Am. S., 322, 67–98, https://doi.org/10.1130/0-8137-2322-1.67, 1998.

Lambe, T.W., and Whitman, R.V.: Soil Mechanics, John Wiley & Sons, New York, 553 pp., ISBN 0471511927, 1969.

Larsen, M.C., and Torres-Sanchez, A.J.: Landslides triggered by hurricane Hugo in eastern Puerto Rico, September 1989. Caribb. J. Sci., 28(3-4), 113–125, 1992.

Larsen, M.C., and Simon, A.: A rainfall intensity-duration threshold for landslides in a humid-tropical environment, Puerto Rico, Geogr. Ann. A, 75(1-2), 13-23, https://doi.org/10.1080/04353676.1993.11880379, 1993.

Larsen, M.C., and Parks, J.E.: Map showing landslide susceptibility in the Comerio municipality, Puerto Rico, U.S. Geol. Surv. Open-File Rep. 98-566, 1 plate, scale 1:20,000. https://doi.org/10.3133/ofr98566, 1998.

Larsen, M.C., and Torres-Sanchez, A.J.: The frequency and distribution of recent landslides in three montane tropical regions of Puerto Rico, Geomorphology, 24(4), 309–331, https://doi.org/10.1016/S0169-555X(98)00023-3, 1998.

Larsen M.C., Santiago, M., Jibson, R., and Questell, E.: Map showing susceptibility to rainfall-triggered landslides in the municipality of Ponce, Puerto Rico, U.S. Geol. Surv. Scientific Investigations Map 2818, 1 plate, scale 1:30,000, https://doi.org/10.3133/sim2818, 2004.

Larsen, M.C.: Landslides and sediment budgets in four watersheds in eastern Puerto Rico, in: Water Quality and Landscape Processes of Four Watersheds in Eastern Puerto Rico, edited by: Murphy, S.F., and Stallard, R.F., U.S. Geol. Surv. Prof. Paper 1789, 153–178, https://doi.org/10.3133/pp1789, 2012.

Lee, S., Ryu, J.-H., Min, K., and Won, J.-S.: Landslide susceptibility analysis using GIS and artificial neural network, Earth Surf. Proc. Land., 28(12), 1361–1376, https://doi.org/10.1002/esp.593, 2003.

1109 Lepore, C., Kamal, S.A., Shanahan, P., and Bras, R.L.: Rainfall-induced landslide susceptibility zonation of Puerto
1110 Rico, Environ. Earth Sci., 66, 1667–1681, https://doi.org/10.1007/s12665-011-0976-1, 2012.
1111 Lepore, C., Arnone, E., Noto, L.V., Sivandran, G., and Bras, R.L.: Physically based modeling of rainfall-triggered
1112 landslides: A case study in the Luquillo forest, Puerto Rico, Hydrol. Earth Syst. Sci., 17(9), 3371–3387,
1113 https://doi.org/10.5194/hess-17-3371-2013, 2013.
1114 Likos, W.J., Wayllace, A., Godt, J., and Lu, N.: Modified direct shear apparatus for unsaturated sands at low suction
1115 and stress, Geotech. Test. J., 33(4), 286–298, https://doi.org/10.1520/GTJ102927, 2010.
1116 Medina, V., Hürlimann, M., Guo, Z., Lloret, A., & Vaunat, J.: Fast physically based model for rainfall-induced
1117 landslide susceptibility assessment at regional scale, Catena, 201, 105213,
1118 https://doi.org/10.1016/j.catena.2021.105213, 2021.
1119 Mergili, M., Marchesini, I., Rossi, M., Guzzetti, F., and Fellin, W.: Spatially distributed three-dimensional slope
1120 stability modelling in a raster GIS, Geomorph., 206, 178-195, https://doi.org/10.1016/j.geomorph.2013.10.008, 2014a.
1121 Mergili, M., Marchesini, I., Alvioli, M., Metz, M., Schneider-Muntau, B., Rossi, M., and Guzzetti, F.: A strategy for
1122 GIS-based 3-D slope stability modelling over large areas, Geosci. Model Dev., 7, 2969–2982,
1123 https://doi.org/10.5194/gmd-7-2969-2014, 2014b.
1124 Mergili, M., Schwarz, L., and Kociu, A.: Combining release and runout in statistical landslide susceptibility modeling,
1125 Landslides, 16(11), 2151–2165, https://doi.org/10.1007/s10346-019-01222-7, 2019.
1126 Metz, C.E.: Basic principles of ROC analysis, Seminars in Nuclear Medicine, 8(4), 283-298,
1127 https://doi.org/10.1016/S0001-2998(78)80014-2, 1978.
1128 Milledge, D.G., Bellugi, D., McKean, J.A., Densmore, A.L., and Dietrich, W.E.: (2015), A multi-dimensional stability
1129 model for predicting shallow landslide size and shape across landscapes, J. Geophys. Res. Earth Surf.,
1130 https://doi.org/10.1002/2014JF003135, 2015.
1131 Montgomery, D.R., and Dietrich, W.E.: A physically-based model for the topographic control on shallow landsliding,
1132 Water Resour. Res., 30, 1153–1171, https://doi.org/10.1029/93WR02979, 1994.
1133 Murphy, S.F., Stallard, R.F., Larsen, M.C., and Gould, W.A.: Physiography, geology, and land cover of four
1134 watersheds in eastern Puerto Rico, U.S. Geol. Surv. Prof. Paper 1789-A, 24 pp., https://doi.org/10.3133/pp1789A,
1135 2012.
1136 Monroe, W.H.: The karst landforms of Puerto Rico, U.S. Geol. Surv. Prof. Paper 899, 69 pp.,
1137 https://doi.org/10.3133/pp899, 1976.
1138 Nicótina, L., Tarboton, D.G., Tesfa, T.K., and Rinaldo, A.: Hydrologic controls on equilibrium soil depths, Water
1139 Resour. Res., 47(4), W04517, https://doi.org/10.1029/2010WR009538, 2011.
1140 Pack, R.T., Tarboton, D.G., and Goodwin, C.N.: The SINMAP approach to terrain stability mapping, in: International
1141 Congress of the International Association of Engineering Geology and the Environment Proceedings, 8th, September
1142 21–25, 1998, Vancouver, British Columbia, Canada, A. A. Balkema, Rotterdam, Netherlands., 2, 1157–1165,
1143 https://digitalcommons.usu.edu/cee_facpub/2583/ 1998.

Palacio Cordoba, J., Mergili, M., and Aristizábal, E.: Probabilistic landslide susceptibility analysis in tropical mountainous terrain using the physically based r.slope.stability model, Nat. Hazards Earth Syst. Sci., 20, 815–829, https://doi.org/10.5194/nhess-20-815-2020, 2020.

Pando, M.A., Ruiz, M.E., and Larsen, M.C.: Rainfall-induced landslides in Puerto Rico: An overview, in: Slopes and Retaining Structures Under Seismic and Static Conditions, edited by Gabr, M.A., Bowders, J.J., Elton, D., and Zornberg, J.G., ASCE Geotech. SP., 140, 2911–2925, https://doi.org/10.1061/40787(166)25, 2005.

Patton, N.R., Lohse, K.A., Godsey, S.E., Crosby, B.T., and Seyfried, M.S.: Predicting soil thickness on soil mantled hillslopes, Nat. Commun., 9, 3329, https://doi.org/10.1038/s41467-018-05743-y, 2018.

Pelletier, J.D., and Rasmussen, C.: Geomorphically based predictive mapping of soil thickness in upland watersheds, Water Resour. Res., 45(9):W09417. https://doi.org/10.1029/2008WR007319, 2009.

Perkins, J.P., Baxstrom, K.W., Einbund, M.M, and Schulz, W.H: Modified basal contact of the Tertiary Lares Limestone in the vicinity of Utuado, Puerto Rico, USA, derived from USGS Open-File Report 98-038, U.S. Geol. Surv. data release [data set], https://doi.org/10.5066/P9NL9EZG, 2022.

Raia, S., Alvioli, M., Rossi, M., Baum, R.L., Godt, J.W., and Guzzetti F.: Improving predictive power of physically based rainfall-induced shallow landslide models: A probabilistic approach, Geosci. Model Dev., 7(2), 495–514, https://doi.org/10.5194/gmd-7-495-2014, 2014.

Ramos-Scharrón, C.E., Arima, E.Y., Guidry, A., Ruffe, D., and Vest B.: Sediment mobilization by hurricane-driven shallow landsliding in a wet subtropical watershed, J. Geophys. Res.-Earth, 126(5), e2020JF006054, https://doi.org/10.1029/2020JF006054, 2021.

Reid, M.E., Christian, S.B., Brien, D.L., and Henderson, S.T.: Scoops3D—Software to analyze 3D slope stability throughout a digital landscape, U.S. Geol. Surv. Techniques and Methods 14-A1 [code], 218 pp. https://doi.org/10.3133/tm14A1, 2015.

Reid, M.E., Coe, J.A., and Brien, D.L.: Forecasting inundation from debris flows that grow volumetrically during travel, with application to the Oregon coast range, USA, Geomorphology, 273, 396–411. https://doi.org/10.1016/j.geomorph.2016.07.039, 2016.

Roering, J.J.: How well can hillslope evolution models “explain” topography? Geol. Soc. Am. Bull., 120(9-10), 1248–1262, https://doi.org/10.1130/B26283.1, 2008.

Rossi, G., Catani, F., Leoni, L., Segoni, S., and Tofani, V.: HIRESSS: a physically based slope stability simulator for HPC applications, Nat. Hazards Earth Syst. Sci., 13, 151–166, doi:10.5194/nhess-13-151-2013, 2013.

Schulz, W.H., Jensen, E.K., Cerovski-Darriau, C.R., Baum, R.L., Thomas, M.A., and Coe, J.A.: Field observations of landslides and related materials following Hurricane Maria, Puerto Rico, U.S. Geol. Surv. data release [data set], https://doi.org/10.5066/P9T9KZ6T, 2023.

Segoni, S., Leoni, L., Benedetti, A. I., Catani, F., Righini, G., Falorni, G., Gabellani, S., Rudari, R., Silvestro, F., and Rebora, N.: Towards a definition of a real-time forecasting network for rainfall induced shallow landslides, Nat. Hazards Earth Syst. Sci., 9, 2119–2133, https://doi.org/10.5194/nhess-9-2119-2009, 2009.

Simon, A., Larsen, M.C., and Hupp, C.R.: The role of soil processes in determining mechanisms of slope failure and hillslope development in a humid-tropical forest eastern Puerto Rico, Geomorphology, 3(3-4), 263–286, https://doi.org/10.1016/0169-555X(90)90007-D, 1990.

Simoni, S., Zanotti, F., Bertoldi, G., and Rigon, R.: Modelling the probability of occurrence of shallow landslides and channelized debris flows using GEOtop-FS, Hydrol. Processes, 22(4), 532–545, doi:10.1002/hyp.6886, 2008.

Smith, J.B., Thomas, M.A., Ashland, F., Michel, A.R., Wayllace, A., and Mirus, B.B.: Hillslope hydrologic monitoring data following Hurricane María in 2017, Puerto Rico, July 2018 to June 2020, U.S. Geol. Surv. data release [data set], https://doi.org/10.5066/P9548YK2, 2020.

Soil Survey Staff: Soil Survey Geographic (SSURGO) Database for Puerto Rico, all regions. U.S. Department of Agriculture Natural Resources Conservation Service [data set], https://websoilsurvey.sc.egov.usda.gov/app/ (last access: 10 August 2023), 2018.

Sowers, G.F.: Landslides in weathered volcanics in Puerto Rico, in: Proceedings of the Fourth Pan-American Conference on Soil Mechanics and Foundation Engineering, American Society of Civil Engineers, New York, 105–115, 1971.

Taggart, B.E., and Joyce, J.: Radiometrically dated marine terraces on northwestern Puerto Rico, in: Transactions of the 12th Caribbean Geological Conference, St. Croix, U.S. Virgin Islands, August 7th-11th, 1989, Miami Geological Society, South Miami, Florida, 248–258, 1991.

Taylor, D.W.: Fundamentals of Soil Mechanics, John Wiley & Sons, New York, 700 pp., 1948.

Thomas, M.A, and Cerovski-Darriau, C.: Infiltration data collected post-Hurricane María across landslide source area materials, Puerto Rico, USA, U.S. Geol. Surv. data release [data set], https://doi.org/10.5066/P9SCGVF7, 2019.

Tello, M.: Optimization of landslide susceptibility modeling: A Puerto Rico case study, Master of Science Thesis, Colorado School of Mines, Golden, Colorado, https://hdl.handle.net/11124/174137, 2020.

Terzaghi, K., Peck, R.B., and Mesri, G.: Soil Mechanics in Engineering Practice, 3rd ed. John Wiley & Sons: New York, 549 pp., ISBN: 978-0-471-08658-1, 1996.

Tofani, V., Bicocchi, G., Rossi, G., Segoni, S., D'Ambrosio, M., Casagli, N., & Catani, F.: Soil characterization for shallow landslides modeling: a case study in the Northern Apennines (Central Italy), Landslides, 14, 755-770, https://doi.org/10.1007/s10346-017-0809-8, 2017.

Turnbull, W.J., and Hvorslev, M.J.: Special problems in slope stability, Journal of the Soil Mechanics and Foundations Division, 93(SM4), 499–528, https://doi.org/10.1061/JSFEAQ.0001004, 1967.

U.S. Geological Survey: 2015–2016 USGS Puerto Rico LiDAR (project PR_PuertoRico_2015) [data set], at https://apps.nationalmap.gov/lidar-explorer/#/ (last access: 10 August 2023), 2018.

U.S. Geological Survey: 2018 USGS Puerto Rico – Virgin Islands LiDAR (project PR_PRVI_A_2018), https://apps.nationalmap.gov/lidar-explorer/#/ (last access: 10 August 2023), 2020a.

U.S. Geological Survey: 2018 USGS Puerto Rico – Virgin Islands LiDAR (project PR_PRVI_D_2018), https://apps.nationalmap.gov/lidar-explorer/#/ (last access: 10 August 2023), 2020b.

U.S. Geological Survey: 2018 USGS Puerto Rico – Virgin Islands LiDAR (project PR_PRVI_H_2018), https://apps.nationalmap.gov/lidar-explorer/#/ (last access: 10 August 2023), 2020c.

von Ruette, J., Lehmann, P. Or, D.: Rainfall-triggered shallow landslides at catchment scale: Threshold mechanics-based modeling for abruptness and localization, Water Resour. Res., 49, 6266–6285, https://doi.org/10.1002/wrcr.20418, 2013.

Wang, S., Zhang K., van Beek, L.P.H., Tian, X., Bogaard, T.A.: Physically-based landslide prediction over a large region: Scaling low-resolution hydrological model results for high-resolution slope stability assessment, Environmental Modelling & Software, 124, 104607, https://doi.org/10.1016/j.envsoft.2019.104607, 2020.

Woodard, J. B., Mirus, B. B., Wood, N. J., Allstadt, K. E., Leshchinsky, B. A., and Crawford, M. M.: Slope Unit Maker (SUMak): an efficient and parameter-free algorithm for delineating slope units to improve landslide modeling, Nat. Hazards Earth Syst. Sci., 24, 1–12, https://doi.org/10.5194/nhess-24-1-2024, 2024.

Wu, W., and Sidle, R.C.: A distributed slope stability model for steep forested hillslopes, Water Resour. Res., 31, 2097–2110, https://doi.org/10.1029/95WR01136, 1995.

Xiao, T., Segoni, S., Liang, X., Yin, K., & Casagli, N.: Generating soil thickness maps by means of geomorphological-empirical approach and random forest algorithm in Wanzhou County, Three Gorges Reservoir, Geoscience Frontiers, 14(2), 101514, https://doi.org/10.1016/j.gsf.2022.101514, 2023.

Yan, Q., Wainwright, H., Dafflon, B., Uhlemann, S., Steefel, C.I., Falco, N., Kwang, J. and Hubbard, S.S.: Hybrid data-model-based mapping of soil thickness in a mountainous watershed, Earth Surf. Dynam. Discuss., 1–23, doi:10.5194/esurf-2020-110, 2021.

Zieher, T., Rutzinger, M., Schneider-Muntau, B., Perzl, F., Leidinger, D., Formayer, H., and Geitner, C.: Sensitivity analysis and calibration of a dynamic physically based slope stability model, Nat. Hazard. Earth Sys., 17(6), 971–992. https://doi.org/10.5194/nhess-17-971-2017, 2017.